UNIVERSITÀ
DI SIENA
1240

Department of Environment, Earth and Physical Sciences
(DSFTA)

PhD Program in Environmental, Geological and Polar Sciences and Technologies (STAGP)

38th Cycle

Coordinator: Prof. Letizia Marsili

Integrated multi-sensor geomatic methodologies for slope stability analysis and monitoring

Scientific disciplinary sector: GEOS-03/B - Applied Geology

PhD Candidate:
Luisa Beltramone[1] Luisa Beltramone

Supervisor:
Prof. Riccardo Salvini[1]

Co-supervisor:
Dr. Andrea Rindinella[1]

Affiliation:
[1]Department of Environment, Earth and Physical Sciences and Center of GeoTechnologies (CGT), University of Siena (Italy)

Academic Year 2024–2025

University of Siena

PhD Program in Environmental, Geological and Polar Sciences and Technologies (STAGP)

38th Cycle

Final examination date

27 April 2026

Scientific board

Prof. Paola Revellino, Department of Science and Technology (DST), University of Sannio, Benevento

Dr. Chiara Caselle, Department of Earth Sciences, University of Turin

Prof. Pier Lorenzo Fantozzi, Department of Physical Sciences, Earth and Environment (DSFTA), University of Siena

Substitute

Prof. Mirko Francioni, Department of Pure and Applied Sciences (DiSPeA), University of Urbino Carlo Bo

Acknowledgements

Desidero esprimere la mia più sincera gratitudine alla mia famiglia “allargata” per il supporto costante, la pazienza e la fiducia che non sono mai venuti meno durante tutto il percorso della mia vita, accademica e non.

Un pensiero speciale va a mia Mamma, Livia, la quale mi ha fatto scoprire l’amore per il territorio ed i fenomeni naturali fin da piccina. Portarmi a vedere l’alluvione del ’94 e i suoi danni in Valle Po, a soli 3 anni, mi ha fatto prendere coscienza della fragilità dell’uomo e del territorio di fronte agli eventi naturali. Il “rombo” costante della corrente del fiume, che trascinava i massi in quelle notti, non ha mai lasciato la mia mente.

Un ringraziamento speciale va anche ai miei amici, da quelli di una vita che mi hanno vista crescere ed affrontare le incertezze della vita, a quelli che mi hanno conosciuta negli ultimi anni, perché con la loro presenza e il loro incoraggiamento hanno reso più leggeri anche i momenti più impegnativi.

Ringrazio i professori e i ricercatori che hanno contribuito alla mia formazione precedente presso l’Università di Torino, l’Università di Vigo (J.P. Harrison Lab) e l’Instituto Superior Técnico (DeCivil) di Lisbona, per aver posto le basi del mio percorso scientifico e personale. Un sentito grazie ai professori e ai colleghi/amici del Centro di Geotecnologie (UniSi) per il confronto quotidiano, la collaborazione e il supporto reciproco, così come a tutto il personale del CGT per la disponibilità e il sostegno nelle attività di ricerca.

Desidero inoltre ringraziare le Reviewers, la Professoressa Revellino e la Dottoressa Caselle, il cui contributo critico ha permesso di migliorare significativamente la qualità

del lavoro, oltre a confermare a me stessa la mia validità in questo campo di ricerca.

Infine, un ringraziamento a me stessa per non aver mollato nei momenti di difficoltà, in cui la sindrome dell'impostore sembrava prendere il sopravvento e farmi mollare tutto, e in cui eventi negativi esterni mi facevano ripensare alle mie scelte. Grazie per aver portato a termine questo percorso con determinazione e resilienza!

Contents

Acknowledgements **1**

1 Introduction **19**

2 Methodologies **23**

2.1 Simultaneous Localization And Mapping (SLAM) 23

2.2 Terrestrial Laser Scanning (TLS) 26

2.3 Unmanned Aerial Vehicle (UAV) photogrammetry 28

2.4 Topographic surveying by Robotic Total Station (RTS) 30

2.5 Topographic surveying by Global Navigation Satellite System (GNSS) 32

2.6 Engineering-geological surveying 34

2.7 Rock Mass Classification 36

2.8 Kinematic stability analysis 38

2.9 Limit equilibrium slope stability analysis 41

2.10 Numerical modeling 43

2.11 Persistent Scatterer Interferometry (PSI) 46

3 Case Studies **48**

3.1 Modeling and stability analysis of the rock mass at the Prehistoric Paglicci Cave system (Italy) 48

3.1.1 Introduction 48

3.1.2 Anthropological and archaeological settings 52

3.1.3 Geological-structural and geomorphological frameworks 54
3.1.4 Seismic framework 56
3.1.5 Materials and Methods 58
3.1.5.1 Topographic survey (GNSS and RTS) 58
3.1.5.2 UAV photogrammetric survey 59
3.1.5.3 SLAM-based LiDAR survey 61
3.1.5.4 Engineering-geological survey 62
3.1.5.5 Rock Mass Classification 64
3.1.5.6 Slope stability analysis 65
3.1.5.6.1 Kinematic stability analysis 65
3.1.5.6.2 Limit equilibrium stability analysis 66
3.1.5.6.3 Numerical modeling 68
3.1.6 Results 72
3.1.6.1 SLAM-based point cloud coregistration and georeferencing 72
3.1.6.2 UAV photogrammetric data processing 73
3.1.6.3 Engineering-geological survey 74
3.1.6.4 Rock Mass Classification 76
3.1.6.4.1 Rock Mass Rating (RMR) method 76
3.1.6.4.2 Q-Slope method 76
3.1.6.4.3 Slope Mass Rating (SMR) method 77
3.1.6.5 Rock slope statistical kinematic stability analysis 79
3.1.6.6 Deterministic kinematic and dynamic stability analysis 81
3.1.6.7 Numerical modeling 83
3.1.7 Discussion 86
3.1.8 Conclusions 91
3.2 Multitemporal slope stability analysis of the Sabereebi rock-cut Monastic Complex (Georgia) 93

3.2.1 Introduction . . . 93
3.2.2 Archeological framework . . . 95
3.2.3 Geological and geomorphological settings . . . 96
3.2.4 Materials and Methods . . . 101
3.2.4.1 Previous data . . . 102
3.2.4.1.1 UAV and Terrestrial Laser Scanning surveys . . . 102
3.2.4.1.2 Geotechnical parameters for FEM simulation . . . 102
3.2.4.2 New data . . . 103
3.2.4.2.1 Terrestrial laser scanning . . . 103
3.2.4.2.2 Unmanned aerial vehicle survey . . . 104
3.2.4.3 Structural discontinuity mapping . . . 105
3.2.4.4 Multitemporal point cloud comparison . . . 106
3.2.4.5 FEM slope stability analysis . . . 108
3.2.5 Results . . . 114
3.2.5.1 Point cloud processing . . . 114
3.2.5.2 Surface change detection from multitemporal point cloud comparison 116
3.2.5.3 FEM modeling for slope stability analysis . . . 118
3.2.5.3.1 Major principal stress (σ_1) distribution . . . 119
3.2.5.3.2 Shear stress (τ) distribution . . . 122
3.2.5.3.3 Vertical displacement (u_z) distribution . . . 125
3.2.5.3.4 Cross-sections analysis . . . 126
3.2.6 Discussion . . . 133
3.2.7 Conclusions . . . 136
3.3 Analysis and monitoring of a vulnerable Vecchiano rock slope (Italy) . . . 138
3.3.1 Introduction . . . 138
3.3.2 Geological setting . . . 142
3.3.3 Material and Methods . . . 143

3.3.3.1 Topographic survey . . . 144
3.3.3.2 UAS photogrammetric survey . . . 146
3.3.3.3 Engineering–geological survey and rock mass characterization . . . 146
3.3.3.4 Statistical slope stability kinematic analysis . . . 147
3.3.3.5 Multitemporal monitoring through RTS . . . 148
3.3.3.6 Persistent Scatterer Interferometry . . . 154
3.3.4 Results . . . 157
3.3.4.1 UAS photogrammetry . . . 157
3.3.4.2 Engineering–geological survey . . . 159
3.3.4.3 Rock Mass Classification . . . 161
3.3.4.4 Statistical kinematic stability analysis . . . 164
3.3.4.5 Multitemporal monitoring through RTS . . . 164
3.3.4.6 Persistent Scatterer Interferometry . . . 170
3.3.5 Discussion . . . 173
3.3.6 Conclusions . . . 177

4 Discussion **179**

4.1 Geological and structural controls on instability . . . 179
4.2 Role of multi-sensor surveying and monitoring . . . 181
4.3 Numerical modeling as interpretative support . . . 183
4.4 Implications for hazard mitigation and heritage conservation . . . 185
4.5 Environmental stressors and climate change context . . . 186
4.6 Synthesis . . . 187

5 Conclusions **190**

5.1 Future research directions . . . 192

6 References **197**

List of Figures

3.1 Cave system of Grotta Paglicci. Archaeological and anthropological findings are marked with colored stars: yellow = 12-m stratigraphy (Middle–Upper Paleolithic sequence); red = Upper Paleolithic wall paintings; blue = external rock shelter (Lower/Middle Paleolithic); purple = Upper Paleolithic sequence outside the present-day entrance; green = Upper Paleolithic deposit. 52

3.2 Panel (A) The red box highlights the location of Grotta Paglicci in relation to the tectonic framework of the study area (modified from **Moretti et al., 2011**). Panel (B) Geological map with 25 m contour intervals (modified from **Moretti et al., 2011**); lithological units are indicated as follows: a—slope cover deposit, b—present alluvial deposit, b2—colluvial deposit, bn—terrace alluvial deposit, CBA_1—Monte Calvo del Gargano Member, CBA_2—Borgo Celano Member. Panel (C) Inset map showing the position of Grotta Paglicci within the Gargano Promontory. 55

3.3 Panel (A) shows the "Seismic classification of the Italian territory" updated to 31 March 2023 (Italian Civil Protection Department, `https://rischi.protezionecivile.gov.it/it/sismico/attivita/classificazione-sismica/`); the green pin indicates the location of Grotta Paglicci. Panel (B) shows the seismic hazard model MPS04-S1 for the Gargano area (source: `https://esse1-gis.mi.ingv.it/`); the black pin indicates the location of Grotta Paglicci within node ID 29447. 56

3.4 Illustrative examples of the different survey stages and targets: GNSS survey (A), RTS survey (B), black–white target for RTS scanning (C), yellow–black target for UAV photogrammetry (D), and circular optical target for SLAM-based LiDAR acquisitions just outside the entrance cave (E). 60
3.5 Acquisition stage in Chamber 2 with the Emesent^{TM} Hovermap ST SLAM-based portable LiDAR. 61
3.6 Survey scan lines used for the engineering–geological investigation, highlighting the outcrops selected for discontinuity and rock mass characterization. 63
3.7 Panel A is an example of various discontinuity orientations measured on the 3D point cloud. Panel B is a detail of the same with the surfaces areas used for orientation measurements highlighted with green parallelepipeds. 64
3.8 New topographic map of the study area from the processing of photogrammetric and SLAM-based LiDAR mapping techniques. Red letters and dotted lines represent the cross-sections used in 2D numerical modeling. . 69
3.9 AA' cross-section; the green and yellow lines represent the main identified joints, while the gray lines indicate the limestone bedding. 71
3.10 BB' cross-section; the yellow and magenta lines represent the main identified joints, while the gray lines indicate the limestone bedding. 72
3.11 CC' cross-section; the yellow and magenta lines represent the main identified joints, while the gray lines indicate the limestone bedding. 72
3.12 (A) Nadiral view of the georeferenced 3D point cloud from SLAM-based LiDAR surveys. Orange dots (EMn) indicate the GCPs used for georeferencing. 73

3.13 (A) Nadiral view of the georeferenced 3D dense point cloud. Blue flags mark the GCPs used for exterior orientation. (B) Nadiral orthophotomosaic. (C) Detail of the frontal orthophotomosaic. 74

3.14 Stereographic projection of discontinuities identified through both the in situ engineering–geological survey and the photointerpretation of geomatic datasets. Orientations are expressed as dip and dip direction, following the right-hand rule, and represented with the Schmidt equal-area method (lower hemisphere). Density variations are indicated by different shades of gray. 75

3.15 Stability chart of the Q-slope method (after **Bar & Barton, 2017**), with the black cross marking the critical stability conditions for an average slope angle of 80°. 77

3.16 Nadiral orthophotomosaic illustrating the orientations of the three slopes (V1, V2, and V3) reported in Table 3.9, which were analyzed using the SMR method (A). On slope V3, examples of kinematic stability assessment are presented through stereographic projections (Wulff equal-angle method, lower hemisphere): planar sliding (B), wedge sliding (C), and direct or oblique toppling (D). The discontinuity sets S1, S2, and S3 correspond to those described in Table 3.9. 78

3.17 The image shows an example of the **Markland Test (1972)** conducted for slope V1 considering the planar sliding mechanism. 80

3.18 Panel (A) and (B) show Block n.1 in front and oblique views. Panel (C) highlights its position relative to the external archaeological excavation area (in purple), with the discontinuity systems that are creating a potentially unstable volume. Panel (D) shows the mesh obtained by CloudCompare software processing(Version 2; **CloudCompare, 2021**) and the planar discontinuities bordering it. 81

3.19 Differential stresses resulting from geotechnical modelling along the AA' cross-section (A). Details of the obtained differential stress values (B). . . 84
3.20 Differential stresses resulting from geotechnical modelling along the BB' cross-section (A). Detail of the obtained differential stress values (B). . . . 85
3.21 Differential stresses resulting from geotechnical modelling along the CC' cross-section (A). Detail of the obtained differential stress values (B). . . . 85
3.22 Displacement values resulting from geotechnical modelling along cross-section AA'. 86
3.23 Displacement values resulting from geotechnical modelling along cross-section CC'. 86
3.24 Main tectonic units and structures of the Eastern Anatolia-Caucasian region superimposed on an ASTER GDEM shaded relief map (from **Gusmeo et al., 2021**). ASASZ = Amasia- Sevan-Akera suture zone; D = Dzirula Massif; IAESZ = Izmir-Ankara-Erzinçan suture zone; K = Khrami Massif; L = Loki Massif; MCT = Main Caucasian Thrust. Red lines with triangles indicate thrusts; red lines are normal, strike-slip or unknown kinematics faults. Inset: Tectonic sketch map of the Arabia-Eurasia collision zone modified after **Cavazza et al. (2019)** and **Sosson et al. (2010)**. EAF = Eastern Anatolian Fault; NAF = Northern Anatolian Fault. 97
3.25 Example of cuesta-type northwest–southeast-trending ridges of the Iori Upland. 97

3.26 Geological Map of the Basin of the Middle Reaches of the Kura River by D. Papava, 1976, scale 1 : 100 000. Stamped: Geological Survey Bureau, State company "Gruzneft", GEOLFOND D1283. **Q** = Quaternary continental unconsolidated alluvial, colluvial, and eluvial deposits. N_2^3**ap** = Apsheronian (Lower Pliocene), continental and marine molasse composed of sands, loams, clays, and sandstones. N_2^3**ak+ap** = Apsheronian–Akchagylian transitional facies, continental and marine molasse including conglomerates, sandstones, clays, loams, and volcanic tuff intercalations. N_2^3**ak** = Akchagylian (Upper Pliocene), continental and marine molasse consisting of conglomerates, sandstones, sands, clays, and volcanic ash intercalations. N_2^1**m+pn** = Meotian and Pontian (Upper Miocene), marine and continental molasse including conglomerates, sandstones, and clays. N_1^3**S1–S3** = Sarmatian (Upper Miocene), marine to continental molasse composed of clays, sandstones, conglomerates, marls, and limestones. N_1^2 = Middle Miocene marine molasse consisting of clays, sandstones, conglomerates (locally with basal conglomerates), marls, oolitic and arenaceous limestones. N_1^1 = Maikop Series (Lower Miocene), marine molasse comprising sandstones, gritstones, weakly carbonaceous clays with marl intercalations, and locally gypsiferous clays and sandstones. **Structural elements**: undifferentiated faults are represented as simple red lines. **Fold axes**: anticline axes are shown with dot–dash lines, whereas syncline axes are represented with dot–dot–dash lines. The black pin marks the location of the Sabereebi Monastery Complex. 99

3.27 Geology of Sabereebi (from **Domej et al., 2022)** 100

3.28 Example of discontinuity extraction: panel (A) shows the visual definition on image; panel (B) shows the sampling on image in Trimble™ Scan Explorer with point cloud as base data for extraction; panel (C) shows, in CloudCompare environment, the georeferenced points, in red, coming from the `*.ASCII` file 106

3.29 Three-dimensional numerical model of the Sabereebi slope and monastic complex developed in RS3. Panel (A) shows the full stratigraphic model with lithological units differentiated by color: topsoil (green), conglomerate (dark red), sandstone (light grey), siltstone (light yellow), and clay (light brown). Panel B shows the internal cave chambers reconstructed from TLS and UAV photogrammetric data and integrated as excavated voids within the sandstone. Panel C shows the planar discontinuities inserted into the sandstone unit based on field observations and 3D interpretation. 113

3.30 Panel A shows the segmented point cloud obtained by processing the TLS data, while panel B shows the point cloud obtained from UAV photogrammetry. Both point clouds are segmented considering the area of interest. . 115

3.31 Results of the M3C2 analysis between 2018 and 2025 point clouds. Colored in green and indicated by red the blocks and detachment areas are shown. 117

3.32 Major principal stress (σ_1) distribution on the Sabereebi cliff, with zoomed views (A, B, and C) showing the localized compressive stress concentrations (range: –0.90 to 4.50 MPa). 121

3.33 Major principal stress (σ_1) distribution around the internal rock-cut chambers. 121

3.34 Zoomed views of the major principal stress (σ_1) distribution around the internal rock-cut chambers. These views highlight stress concentrations along the lower margins of the excavated volumes. Panel A shows the northwestern chamber, panel B shows its neighbor chamber towards southeast, panel C shows the central chamber, and panel D shows the southeastern most chambers. 122

3.35 Shear stress (τ) distribution on the Sabereebi cliff, with zoomed views (A, B, C, and D) showing the localized shear stress concentrations (range: 0 to 2.50 MPa). 123

3.36 Shear stress (τ) distribution in correspondence with the excavated chambers showing the localized shear stress concentrations. 124

3.37 Views of shear stress (τ) distribution in correspondence with the excavated chambers showing the localized shear stress concentrations. Panels A1 and A2 show the first two chambers from NW, panels B1 and B2 show the central chamber, and panels C1 and C2 show the two southeastern most chambers. All chambers are shown from two different points of view. . . . 124

3.38 Vertical displacement (u_z) distribution on the Sabereebi cliff. 125

3.39 Vertical displacement (u_z) distribution in correspondence with the excavated chambers showing the localized variations. 126

3.40 Vertical displacement (u_z) distribution around the internal rock-cut chambers. Panel A shows the northwestern chamber, panel B shows its neighbor southwestern chamber, panel C shows the central chamber, and panel D shows the southeastern most chambers. 126

3.41 Set of thirteen FEM cross-sections: seven longitudinal sections aligned with the chamber axis (A) and six inward-oriented slices parallel to the façade (B). 127

3.42 Set of seven cross-sections orthogonal to the cliff showing the major principal stress (σ_1) distribution. 128
3.43 Set of six cross-sections parallel to the cliff showing the major principal stress (σ_1) distribution. 129
3.44 Set of seven cross-sections orthogonal to the cliff showing the shear stress (τ) distribution. 130
3.45 Set of six cross-sections parallel to the cliff showing the shear stress (τ) distribution. 131
3.46 Set of seven cross-sections orthogonal to the cliff showing the shear stress (u_z) distribution. 132
3.47 Set of six cross-sections parallel to the cliff showing the shear stress (u_z) distribution. 133
3.48 Geology of the investigated area. (A) General location of the site in Italy; (B) regional setting based on Sheet no. 273 "Pisa," adapted from **Carosi et al., 2021**; (C) extract of the same geological sheet (**Carosi et al., 2021**). The study site is highlighted with a red star. 142
3.49 Overall methodology flowchart. 144
3.50 Stages of the GNSS (A) and RTS surveys (B). 145
3.51 Images in panels (A) and (B) illustrate representative outcrops chosen for the in situ engineering–geological investigations. In panel (C), yellow dashed lines mark the position of the scanlines along the slope, while red rectangles highlight the portions of rock mass where discontinuity sampling was carried out using CloudCompare software. 146
3.52 Panel (A) shows the Robotic Total Station (RTS) mounted on a steel plate anchored to a reinforced concrete curb. Panel (B) presents the rock walls observed from the RTS station, while panel (C) depicts the macroprism and microprism employed during the multitemporal RTS monitoring campaigns. 149

3.53 The RTS base is marked in yellow together with the distribution of the prisms. The green symbols correspond to the reference prisms adopted to orient the monitoring setup, whereas the red ones represent the monitoring prisms repeatedly measured throughout the nine multitemporal survey sessions. 150
3.54 Example of error ellipse for the B4 monitoring prism. 154
3.55 Metallic corner reflectors positioned along the upper edge above the rock walls: (A) map of reflector locations in the study area; photographs CR1, CR2, and CR3 illustrate detailed views of the installed devices. 155
3.56 (A) Strip of satellite images of the study area; (B) corresponding satellite view of the same extent. The yellow squares highlight the area of interest. 157
3.57 (A) Perspective view of the scaled and georeferenced 3D point cloud of the rock walls (scale bar valid for A only); (B) georeferenced orthophotomosaic of the rock walls and adjacent alluvial plain. 158
3.58 Stereographic projection (Schmidt equal-area method—lower hemisphere) of data collected during the in situ engineering–geological survey. 159
3.59 Stereographic projection (Schmidt equal-area method—lower hemisphere) of data interpreted on the 3D point cloud. 160
3.60 Slopes analyzed with the SMR method and subsequent statistical kinematic stability assessment (see Section 3.3.4.4). Stereographic projections (Wulff equal-angle, lower hemisphere) illustrate an example of the kinematic analysis, here represented by a wedge sliding case. 162
3.61 Plan view of the multitemporal monitoring results (prisms B1–B15). Orange ellipses represent the error associated with each prism, while colored points indicate the nine survey campaigns. 166

3.62 Plan view of multitemporal monitoring results for prisms B16–B30. Error ellipses are shown in orange, and colored points correspond to the nine survey campaigns. 167
3.63 Differential slope distance (A) and vertical displacement (B) of prisms measured in all RTS surveys. Red vertical bars mark the uncertainty thresholds for each prism. 168
3.64 Differential slope distance (A) and elevation displacement (B) of each prism as computed with respect to R4. The uncertainty thresholds for each prism are indicated by the red vertical bars. 169
3.65 PSI results expressed as LOS velocities (mm/yr) for Sentinel-1A (A) and Sentinel-1B (B). Yellow squares mark the artificial corner reflectors installed on the top of the rocky slopes, while the blue triangle indicates the building hosting the RTS. 171
3.66 PSs detected by the LaMMa regional interferometric service in the study area. The red circle highlights point FV6XKKY near the RTS. The lower diagram displays the LOS velocity trend (mm/yr) for this PS over the RTS monitoring period. Light blue ellipses mark the acquisition dates of the 7^{th} and 8^{th} RTS surveys. 172
3.67 Differential slope distance (A) and elevation displacement (B) of each prism as measured during the survey conducted on 4 March 2024. 176

4.1 Proposed generalized workflow for slope stability analysis, illustrating the integration of geomatic and geomechanical methods and key decision-making steps. 188

List of Tables

3.1 Seismic parameters for the Grotta Paglicci area. 57
3.2 Values of JCS, JRC, and φ_r used for the characterization of discontinuities considered in the deterministic dynamic analysis of the identified blocks. . 67
3.3 Partial factors defined by Eurocode 7 EN 1997 for Approach 1 - Combination 2. 67
3.4 Engineering–geological attributes of the modeled rock material. 70
3.5 Engineering–geological characteristics of the discontinuity systems. . . . 71
3.6 Engineering–geological parameters of the identified discontinuity systems. 75
3.7 Shear strength parameters and deformation modulus (E), calculated according to **Bieniawski (1989)**. 76
3.8 Slope dip angle values required to accept different probabilities of failure (PoF) according to the Q-slope method (**Bar & Barton, 2017**). 77
3.9 Average values of dip direction and dip of discontinuity systems and slopes used to verify potential instabilities. 78
3.10 Results of the SMR method application for the three analyzed slopes (V1, V2, and V3). Critical values are marked with an asterisk. 79
3.11 Results of the kinematic slope stability analysis. 80
3.12 Geometrical attributes of blocks n.1 and n.2 in terms of Dip Direction (DipDir) and Dip. 81
3.13 Kinematic stability results for blocks n.1 and n.2. 82

3.14 Deterministic dynamic analysis results of blocks n.1 and n.2 for direct/oblique and flexural toppling. 82
3.16 Deterministic dynamic analysis results of Block n.1 for planar sliding. . . 83
3.17 Geotechnical parameters of lithologies present in the Sabereebi Cave Monastery area (modified from **Domej et al., 2022**). 103
3.18 Parameters assigned to the sandstone unit modelled with the generalized Hoek–Brown criterion (**Hoek et al., 2002**). 110
3.19 Geotechnical parameters chosen as input for the FEM simulation (Mohr–Coulomb = MC; Generalized Hoek–Brown = GHB). 111
3.20 Summary of the assigned joint parameters according to the Barton–Bandis model (**Barton & Bandis, 1990**). 113
3.21 Volumes of detached material between 2018 and 2025 derived from M3C2-based segmentation and *Poisson Surface Reconstruction*. 118
3.22 Summary of the final uncertainty threshold values for each monitoring prism. 152
3.23 Information on the SAR data utilized in the PSI analysis. 157
3.24 Characteristics of discontinuity systems derived from field surveys and 3D point cloud photointerpretation. 161
3.25 Results of the SMR method application with reference to the six analyzed slopes, as shown in Figure 3.60. (P = planar failure, W = wedge failure, and T = toppling). 163
3.26 Results of the kinematic stability analysis for the six representative slopes. (P = Planar sliding; W = Wedge sliding; DT = Direct toppling; FT = Flexural toppling). 164
3.27 Summary of the average precision values for each RTS monitoring survey. 165

Chapter 1

Introduction

Slope instability, occurring as rockfalls, landslides, and related processes, represents one of the most significant natural hazards affecting both natural and anthropogenic settings. These phenomena not only endanger infrastructure and communities but also place irreplaceable archaeological and cultural heritage at risk. Approaching such hazards requires an integrated methodology that combines classical engineering-geological fieldwork with modern monitoring technologies and numerical analysis.

Over the last two decades, geospatial and remote sensing techniques have advanced considerably, offering new possibilities for documenting and understanding slope stability processes. In particular, the increasing use of Simultaneous Localization and Mapping (SLAM), Terrestrial Laser Scanning (TLS), Unmanned Aerial Vehicles (UAVs), and satellite-based interferometric synthetic aperture radar (InSAR) has allowed researchers to capture deformation with unprecedented resolution. UAV-based photogrammetry, for example, has proven highly flexible for mapping inaccessible rock slopes and extracting discontinuity sets (**Cirillo et al., 2024**; **Minervino Amodio et al., 2024**; **Žabota & Kobal, 2021**). Similarly, TLS has been widely applied to quantify rockfall volumes and monitor morphological change over time (**Chen et al., 2025**). At a lower scale, InSAR techniques enable continuous monitoring of ground displacement across wide areas, supporting the

detection of slope displacements that may otherwise go unnoticed (**Bar & Dixon, 2021**; **Bovenga et al., 2022**; **Manconi et al., 2024**).

During field campaigns, often it is required to adapt the choice of technique depending on accessibility, vegetation cover, or the vulnerability of the site under investigation, reminding that, while the methods are powerful, their application is rarely straightforward.

Engineering-geological classification systems remain essential in bridging observations and modeling. Rock Mass Rating (RMR, **Bieniawski, 1973**), Slope Mass Rating (SMR, **Romana, 1985**), and Q-Slope (**Bar & Barton, 2017**) continue to provide a reliable framework for deriving input parameters when laboratory data are unavailable (**Romana et al., 2015**; **Somodi et al., 2021**). In practice, these systems are still indispensable for constraining numerical models in contexts where direct mechanical testing is impossible, particularly in heritage sites where sampling must be kept to a minimum.

Numerical modeling itself serves as the link between empirical observations and predictive capability. The Finite Element Method (FEM) and related approaches have been widely applied to simulate failure mechanisms and assess stability conditions (**Erharter et al., 2024**). In this thesis, models have not been used as absolute predictors but as scenario-testing frameworks, helping to interpret field data and anticipate the consequences of different instability mechanisms.

This research focuses on three case studies that reflect both the diversity of slope environments and the adaptability of methodological approaches:

- Grotta Paglicci (Foggia, Italy): A Paleolithic cave site, where the conservation of archaeological deposits and artworks requires careful assessment of surrounding rock stability.
- Vecchiano (Pisa, Italy): An inhabited slope where rockfalls pose direct risks to infrastructure and local communities.
- Sabereebi Monastic Complex (Georgia): A rock-cut religious site, vulnerable to

progressive volumetric changes that threaten both its structural integrity and cultural value.

The three case studies considered in this research involve rock masses characterized by markedly different mechanical behaviors, ranging from jointed carbonate rocks (Grotta Paglicci and Vecchiano) to weak sedimentary formations (Sabereebi Monastic Complex).

Such variability requires not only different investigation strategies, but also different conceptual approaches to geomechanical characterization and slope stability analysis. In jointed rock masses, instability is primarily governed by the geometry and mechanical properties of discontinuities, making structural surveys and kinematic analyses essential tools. In contrast, weak rocks tend to behave as continuous or equivalent continua, where the overall rock mass properties play a dominant role. This distinction directly influences both the selection of geomatic and topographic survey techniques and the choice of modeling approaches adopted throughout this work, highlighting the need for flexible and context-dependent methodologies in slope stability assessment.

The main objectives of the thesis are to:

- Apply empirical classification systems (RMR, SMR, Q-Slope) as inputs for stability analysis.
- Assess the performance of monitoring techniques (RTS, PSI, TLS, SLAM, UAV photogrammetry) under varying site-specific conditions.
- Apply numerical models to unify field data and monitor observations into stability scenarios.
- Explore how these integrated approaches can inform both hazard mitigation and heritage conservation strategies.

The structure of the thesis reflects these aims. The opening chapters introduce the theoretical and methodological background, followed by a detailed presentation of each case

study. The discussion chapter synthesizes cross-cutting insights, while the conclusions summarize contributions, limitations, and directions for future research. In short, this thesis aims to show that modern geospatial and engineering-geological approaches, when adapted to local conditions, can contribute not only to improved slope hazard assessment but also to protect and preserve vulnerable cultural landscapes.

Chapter 2

Methodologies

2.1 Simultaneous Localization And Mapping (SLAM)

Simultaneous Localization and Mapping (SLAM) is a mobile mapping technology that enables a sensor platform to determine its position while generating a spatially consistent representation of its surroundings (**Smith & Cheeseman, 1986**). Unlike static Terrestrial Laser Scanning (TLS), which requires multiple fixed scan stations and post-acquisition registrations, SLAM facilitates continuous acquisition during operator movement, allowing real-time mapping even in complex environments (**Chen et al., 2022**; **Cheng et al., 2022**).

SLAM systems integrate complementary sensors to achieve this functionality. LiDAR produces dense three-dimensional point clouds, the Inertial Measurement Unit (IMU) records acceleration and angular velocity for motion and position estimation, and visual sensors (RGB or RGB-D) capture texture and color information for feature recognition (**Chen et al., 2018**). An RGB-D image is a combination of an RGB image and its corresponding depth image, better known as a depth map. Depth maps are 2D grayscale images of the same size as the RGB ones they are associated with. The gray level of each pixel of the depth map indicates the distance to the camera of its corresponding RGB

pixel. In the depth map, each pixel sets the position in the Z-axis of the corresponding RGB pixel. The 0 value of the depth pixels corresponds to the farthest points of the 3D scene from the capture camera. The value 255 means that the pixels are located at the nearest planes.

In robotic applications, wheel encoders or odometers may also be incorporated in a SLAM for displacement tracking. The integration of these sensors allows the SLAM algorithm to identify distinctive environmental features, associate new measurements with previously acquired data, estimate the position and orientation of the scanner, and apply loop closure corrections when previously mapped areas are revisited (**Labbé & Michaud, 2014**; **Guivant & Nebot, 2001**; **Thrun et al., 2004**).

This technology is particularly advantageous in environments where GNSS is unavailable or unreliable, such as caves, tunnels, and dense indoor spaces (**Bresson et al., 2017**). In such cases, TLS surveys require numerous stationary setups with significant overlap for registration, making them time-consuming and logistically demanding. By contrast, SLAM enables rapid, uninterrupted data capture without repeated repositioning, reducing field time and manpower requirements while providing immediate visual feedback on acquisition quality.

In this research, SLAM was employed for surveying Grotta Paglicci, an archaeological and paleoanthropological site characterized by narrow passages, irregular chamber geometries, and variable lighting conditions. These constraints limit the feasibility of TLS. A handheld LiDAR-based SLAM survey was carried out through the cave along pre-planned acquisition paths to ensure adequate coverage and feature overlap. Strategic loop closures were incorporated into the scanning trajectory to mitigate positional drift. Multiple passes from different angles reduced occlusions and improved the completeness of the final model.

Although efficient, SLAM is subject to accuracy limitations. The most significant is cumulative drift in position estimation over long trajectories, which can lead to geometric

distortions. This is partially corrected by loop closure but remains problematic in low-feature environments such as smooth rock walls (**Engel et al., 2018**). Performance may also be degraded by reflective or wet surfaces, poor lighting for visual-based systems, and transient elements in the scene (**Tian et al., 2019**).

In this study, these limitations were mitigated through careful trajectory planning, repeated scanning of critical sections, and the use of GNSS-derived control points for georeferencing and validation.

Recent advances in SLAM include the integration of LiDAR, visual, and inertial data in hybrid systems, the application of deep learning for semantic feature recognition and robust loop closure detection, and the adoption of cloud-based processing for improved efficiency (**Wang et al., 2017**; **Chen et al., 2022**). These developments are progressively enhancing SLAM's robustness in challenging survey conditions, supporting its role as a valuable complement to TLS in geological and cultural heritage documentation.

2.2 Terrestrial Laser Scanning (TLS)

Terrestrial Laser Scanning (TLS), also known as terrestrial or topographic LiDAR, is a ground-based remote sensing technique that allows to acquire dense three-dimensional point clouds by emitting laser pulses towards surfaces and measuring their return time or phase shift (**Vosselman & Maas, 2010**). Unlike airborne LiDAR, TLS captures highly detailed spatial data from static positions on the ground, making it particularly suitable for applications in geosciences, engineering, and cultural heritage documentation (**Telling et al., 2017**).

TLS instruments operate according to three main measurement principles (**Boehler et al., 2003**; **Vosselman & Maas, 2010**):

- Time-of-Flight (ToF) scanners calculate distances by measuring the travel time of laser pulses, offering long-range capability but lower precision at close distances.
- Phase-Shift (PS) scanners measure the phase difference between emitted and received continuous waves, providing higher accuracy at short to medium ranges.
- Triangulation-based scanners project a laser spot onto a surface and use optical sensors to determine distance by triangulation, achieving sub-millimetric accuracy at very short ranges, but are limited to a few meters.

The advantages of TLS are well established: it provides millimetric to centimetric accuracy, with typical errors in the order of 2–6 mm up to distances of 50 m (**Kersten & Lindstaedt, 2022**). Its ability to rapidly generate dense point clouds enables detailed reconstruction of complex geometries such as cliffs, slopes, façades, or archaeological sites and structures. TLS is widely used for geomorphic change detection, slope stability analysis, and structural monitoring in built heritage (**Telling et al., 2017**; **Tarsha Kurdi et al., 2023**).

However, TLS also presents limitations: because it relies on direct line-of-sight, multiple scans are often needed to mitigate occlusions caused by vegetation, terrain irregularities, or architectural features. Instruments are relatively bulky, require tripod setup and stable platforms, and are sensitive to environmental conditions such as humidity or surface reflectivity. In addition, large point clouds demand substantial computational resources for registration, filtering, and georeferencing, often requiring specialized software and expertise (**Telling et al., 2017**; **Tarsha Kurdi et al., 2023**).

In this thesis, TLS was employed for high-precision documentation and monitoring where geometric fidelity was essential, notably for the multi-temporal surveys of the Sabereebi Monastic Complex. The limitations mentioned above were solved by organizing surveys with an elevated number of stations positioning and integrating the UAV surveys' outputs to have a comprehensive model. Detailed acquisition strategies, registration procedures, and validation metrics are presented in the corresponding case study chapters.

2.3 Unmanned Aerial Vehicle (UAV) photogrammetry

Unmanned Aerial Vehicles (UAVs) have become an essential tool in geomatics, enabling the acquisition of high-resolution spatial data in areas where terrestrial methods are limited by accessibility or safety concerns. Their use has grown rapidly in geosciences, with relevance to landslide and slope stability assessment (**Colomina & Molina, 2014**; **Nex & Remondino, 2014**; **Sun et al., 2024**). In general, UAVs are divided in two categories: fixed-wings and multirotor. While the first type is more adapt for large-scale spatial acquisitions in nadiral mode, the second is more suitable for small-scale mapping that requires also oblique acquisitions (e.g., vertical elements such as cliffs and steep slopes).

Among several sensors that may be mounted on a drone (multispectral, hyperspectral, thermal, radar cameras, etc.) UAV RGB photogrammetry provides centimetric-scale digital products, such as dense point clouds, orthophotomosaics, and digital elevation models (DEMs), that support geomorphological and geotechnical analyses, often with a level of detail that surpasses conventional aerial surveys (**Bemis et al., 2014**; **Cook, 2017**). When flight planning ensures adequate image overlap, Structure-from-Motion techniques (SfM, **Spetsakis & Aloimonos, 1991**) enable precise 3D reconstructions suitable for defining slope geometry, discontinuity attitudes, spacing, persistence, termination, and, in such cases, joint surface roughness (**Salvini et al., 2020**). Multi-temporal surveys are particularly valuable for documenting surface change, with recent research showing that UAV photogrammetry can achieve centimeter-level accuracy in detecting small-scale deformations when compared to GNSS benchmarks (**Zhang et al., 2024**).

The integration of UAV datasets with ground-based technologies enhances the robustness of slope investigations. By combining UAV photogrammetry with Terrestrial Laser Scanning (TLS) and Simultaneous Localization and Mapping (SLAM), it is possible to overcome line-of-sight restrictions and obtain comprehensive 3D models of complex

slopes. UAV photogrammetry has also proven effective for rockfall analyses, where detailed 3D reconstructions are used to assess slope stability and block volumes (**Cirillo et al., 2024**). In cultural heritage contexts, UAVs support rapid, non-invasive documentation of sites exposed to geological hazards, providing data for both conservation and risk mitigation (**Caciora et al., 2024**).

Nevertheless, UAV surveys are subject to limitations: battery-powered multirotor UAVs, which are most commonly employed in geomatic and slope-monitoring research, typically have a flight autonomy of only 20–40 minutes, and data acquisition is sensitive to weather conditions such as wind, rain, or fog. In addition, aviation regulations constrain operations through requirements for line-of-sight flights and airspace restrictions (**Stöcker et al., 2017**).

Despite these challenges, ongoing developments in sensor miniaturization, battery technology, and automated processing workflows are steadily increasing the reliability and efficiency of UAV systems. Given these advances, UAV photogrammetry is expected to remain a cornerstone technology in slope stability analysis and in the protection of cultural heritage at risk from geohazards.

2.4 Topographic surveying by Robotic Total Station (RTS)

Robotic Total Stations (RTS) are an advanced evolution of traditional total stations, integrating Automatic Target Recognition (ATR), motorized drives, and remote control to allow for precise and continuous monitoring without the constant presence of an operator. Unlike manual total stations, RTS can automatically detect and track surveying prisms, significantly improving efficiency, safety, and reliability in geodetic tasks. Their role has expanded from classic topographic surveys to long-term monitoring of natural and man-made slopes, structural health assessment, and open-pit mine control, where high-frequency and high-precision measurements are essential (**Glueer et al., 2021**).

The operating principle of RTS builds upon the integration of three key components: a theodolite for angular measurements, an Electronic Distance Meter (EDM) for calculating distances to a prism, and servomotors that allow the instrument to reorient automatically. The ability to maintain prism lock is made possible by ATR technology, which relies on the reflective properties of surveying prisms. As described by **Leica Geosystems (2015)**, prism geometry and coating determine signal strength and return quality, directly influencing the measurement accuracy and the stability of tracking over long periods. This explains why instrument–prism configurations are carefully selected depending on environmental conditions and monitoring requirements.

Beyond conventional angle and distance measurements, modern RTSs have evolved into true multi-sensor platforms. The Leica Nova MS50, for example, combines RTS functionalities with 3D laser scanning and high-resolution imaging, enabling both geodetic precision and dense spatial documentation from the same instrument (**Leica Geosystems, 2013**). This integration has opened new possibilities for combining geometric monitoring with detailed surface modelling in a single workflow.

The use of RTS in applied geoscience has been particularly successful in open-pit mining environments. **Long et al. (2018)** demonstrated the ability of RTS to deliver

accurate control of mine wall surfaces, where results were compared with TLS-derived models. Their study confirmed that RTS can achieve millimetric precision in monitoring tasks, providing an essential complement to terrestrial laser scanning by supplying targeted, time-series data. Such integration enhances both the reliability and the interpretability of slope monitoring in high-risk contexts.

Recent studies have extended these applications to natural and cultural heritage slopes: **Glueer et al. (2021)** highlighted the challenges and solutions of deploying RTS in high-alpine environments, while **Beltramone et al. (2024)** demonstrated its value in multitemporal monitoring of rocky walls, integrating RTS observations with Persistent Scatterer Interferometry for slope stability assessment.

The advantages of RTS can be summarized as follows: high accuracy, automation, real-time capability, and reduced need for direct operator intervention in hazardous areas.

However, limitations remain: RTS monitoring requires uninterrupted line-of-sight to prisms, making network design critical in complex topographies. Data quality may also be affected by adverse atmospheric conditions, such as fog or heavy precipitation, and long-term projects require careful maintenance and calibration of both instruments and prisms.

In this thesis, RTS was employed in two complementary ways. At Paglicci Cave, RTS was used to establish a geodetic control network that provided accurate georeferencing of TLS, UAS photogrammetry, and SLAM surveys in a complex archaeological location. At Vecchiano, RTS was integrated into a long-term strategy for slope stability monitoring, delivering continuous, high-precision displacement data and validation of satellite-based measurements. These applications illustrate the versatility of RTS and confirm its role as a key instrument for geomorphological and heritage monitoring.

2.5 Topographic surveying by Global Navigation Satellite System (GNSS)

Global Navigation Satellite System (GNSS) surveying has become a fundamental method in geosciences, providing high-precision positioning for geodetic control, slope stability investigations, and structural monitoring. Unlike traditional terrestrial instruments, GNSS offers continuous, absolute positioning across large areas, enabling the detection of both rapid and long-term displacements. Recent advances have further expanded GNSS applications in landslide and slope monitoring, with studies demonstrating its ability to capture real-time deformation processes and provide reliable early-warning information (**Huang et al., 2023**; **Tao et al., 2024**).

GNSS refers to the ensemble of satellite constellations, including NAVSTAR GPS (United States), GPS (United States), GLONASS (Russia), Galileo (Europe), and BeiDou (China). Modern survey-grade receivers can track signals from multiple constellations and frequencies, significantly reducing errors caused by atmospheric delays, multipath effects, or satellite clock inaccuracies (**Teunissen & Khodabandeh, 2022**; **Li et al., 2022**). By measuring the travel time of signals from at least four satellites, receivers compute three-dimensional positions with metric to millimetric accuracy, depending on the positioning mode (autonomous, differential, static, RTK/NRTK) and on whether data are processed in real time or through post-processing techniques.

Different GNSS methodologies are applied depending on survey objectives. Static positioning, typically carried out in differential mode using Continuously Operating Reference Stations (CORS), achieves millimetric precision and is well-suited for long-term deformation monitoring (**Notti et al., 2020**). Precise Point Positioning (PPP) and its evolution into PPP–RTK integrate precise orbit and clock products with network corrections, enabling real-time centimetric accuracy over wide regions (**Teunissen & Khodabandeh,**

2022; **Li et al., 2022**). Network Real-Time Kinematic (NRTK) systems, based on dense CORS infrastructures, are increasingly employed in engineering and geohazard contexts, with proven reliability in high-latitude and challenging terrain conditions (**Wang et al., 2022**; **Jacobsen et al., 2023**).

The advantages of GNSS include continuous, absolute positioning that is independent of line-of-sight constraints and scalable across local to regional networks. Low-cost receivers have recently been validated for continuous slope monitoring, making the technique accessible for long-term campaigns in both natural and cultural heritage settings (**Hamza et al., 2023**). Furthermore, advanced GNSS networks deployed in open-pit mines and unstable slopes demonstrate the ability to detect subtle quasi-static deformations and predict displacements when enhanced by machine learning and graph-based optimisation techniques (**Li et al., 2025**).

Nevertheless, GNSS performance can be degraded in obstructed environments such as narrow valleys, forests, or cave entrances, where multipath and signal blockage prevent the measurements or reduce accuracy. Atmospheric conditions also introduce errors; however, these are adequately mitigated through differential processing with CORS, especially when longer observation periods are considered, as well as by dual-frequency, multi-constellation receivers and augmentation services (**Huang et al., 2023**).

In this thesis, GNSS served as a supporting method for slope stability investigations. At Paglicci Cave, GNSS was employed to establish ground control points for the georeferencing of UAV acquired images, TLS and SLAM datasets. At Sabereebi, GNSS supported the alignment and georeferencing of multi-temporal TLS acquisitions of the monastic complex. At Vecchiano, GNSS observations validated the RTS monitoring network and provided an independent reference frame for the RTS monitoring network and the displacement measurements.

These applications highlight GNSS as a robust geodetic backbone for multi-sensor integration, ensuring spatial consistency and accuracy across the diverse case studies.

2.6 Engineering-geological surveying

Engineering–geological surveys form the foundation of geotechnical investigation in rocks, as they provide essential information on the geological, structural, and mechanical characteristics of rock masses. They are not only a descriptive step in site characterization, but also a diagnostic and interpretative tool that supports hazard assessment and the design of mitigation strategies.

The goal is to translate field and laboratory observations into geotechnical parameters that can be employed in both empirical and numerical models of slope stability (**Goodman, 1989**; **Hoek & Bray, 1981**).

Traditionally, these surveys rely on direct field observations and manual measurements of lithological and structural features. In particular, discontinuity mapping is a key task, since parameters such as joint orientation, spacing, persistence, aperture, roughness, and infilling strongly influence rock mass behavior and the development of instability mechanisms (**Wyllie & Mah, 2004**). Such surveys have the advantage of capturing large-scale qualitative attributes (roughness, weathering, infill), but they are constrained by accessibility and safety issues and are inherently subject to observer bias (**Priest, 1993**; **Hudson & Harrison, 1997**).

In this work, discontinuity data were acquired using a combined approach. Traditional field surveys allowed the collection of structural measurements at representative and accessible outcrops. In parallel, high-resolution three-dimensional point clouds obtained from TLS and UAV-based photogrammetry were analyzed through the CloudCompare software.

Its Compass plugin's Plane Tool was used to extract best-fit planes from selected portions of the point cloud, providing dip and dip-direction values. This method enabled the characterization of discontinuity attitudes even in inaccessible or unsafe areas, thereby expanding spatial coverage and reducing operator bias (**Gigli & Casagli, 2011**; **Riquelme**

et al., 2014).

Recent applications have demonstrated that TLS and photogrammetry allow semi-automatic detection of discontinuity attitude, spacing, termination, and persistence with high reliability, though resolution limits may prevent the identification of small apertures, surface roughness, or thin infills (**Assali et al., 2014**). Moreover, least-squares plane fitting assumes planarity, which may oversimplify irregular or curved surfaces (**Riquelme et al., 2014**).

Beyond discontinuity mapping, the engineering–geological surveys also addressed lithological variability, weathering conditions, hydrogeological settings, and geomorphological features such as scarps, debris deposits, and evidence of past slope displacements. This multi-scale perspective ensured that geological, structural, and surface-process controls on slope stability were jointly considered. At the same time, these surveys provide only a static representation of slope conditions. Temporal evolution and deformation processes require integration with monitoring methods, such as those of the Geomatics field (**Lato et al., 2009**).

Overall, the integration of classical and digital techniques provided a comprehensive dataset that underpinned the subsequent rock mass classifications, stability analyses, and stress-strain numerical modelling. The main advantage of this hybrid approach lies in combining the detail and qualitative insight of fieldwork with the coverage and repeatability of digital models, while the main limitation is a possible generalization of complex rock mass behavior into empirical parameters.

2.7 Rock Mass Classification

Empirical rock mass classification systems remain a cornerstone of engineering geology, providing a semi-quantitative framework for evaluating rock mass quality and its implications for stability. They originated in the 1970s with the recognition that structural, lithological, and hydrogeological parameters could be systematically scored and combined to characterize rock mass behavior (**Bieniawski, 1973**; **Barton et al., 1974**).

Despite their apparent simplicity, these systems have endured because they offer a pragmatic means of translating complex geological conditions into engineering decisions.

Among the systems most relevant to slope stability are the Rock Mass Rating (RMR), the Q-Slope system, and the Slope Mass Rating (SMR). Each provides a different perspective on rock mass quality, reflecting the diversity of engineering challenges encountered in rock slope analysis.

RMR, developed by **Bieniawski (1973)**, is probably the most widely adopted. It integrates intact rock strength, discontinuity quality, groundwater conditions, and orientation effects into a 0–100 index. Its longevity lies in its versatility: it can be applied across tunneling, dam foundations, open pits, and natural slopes. However, its generalized scoring means that site-specific variability is sometimes under-represented, and its categorical thresholds do not always capture continuous variations in rock mass properties (**Palmstrøm & Broch, 2006**).

By contrast, Q-Slope (**Bar & Barton, 2017**) is a more recent adaptation of the tunneling Q-system, and it was designed specifically for rock slopes. It incorporates discontinuity characteristics, number, groundwater, and slope-related stress factors into a multiplicative expression that correlates with allowable slope angles and failure probabilities. Its strength is that it links rock mass quality directly to slope geometry, thereby bridging structural observations and practical slope design.

Nevertheless, as highlighted by **Alejano (2024)**, all empirical rock mass classification

systems require careful adaptation to local conditions, and even with the expanded database of over 600 case studies presented by **Bar and Barton (2024)**, the Q-Slope method continues to undergo refinements — such as updated stability charts and time-dependent factors — underscoring the limits of its universality.

SMR, introduced by **Romana (1985)**, extends RMR by applying correction factors for discontinuity orientation in relation to that of the slope. This makes it especially powerful for evaluating structurally controlled instabilities, such as planar, wedge failures, and toppling. In practice, SMR is particularly valuable in road cuts, quarries, and other excavated slopes, where excavation method and slope orientation strongly influence stability (**Romana et al., 2003**). Its limitation, however, lies in the subjectivity of some correction factors, which can lead to variability between practitioners.

In this thesis, these three classification systems were applied in a complementary manner.

RMR was used to provide a baseline measure of rock mass quality, independent of slope context.

Q-Slope was applied to explicitly evaluate slope stability potential, linking rock mass characteristics with slope angle and probability of failure.

SMR was employed to account for the geometric interaction between discontinuities and slope orientation, refining the stability assessment for structurally controlled failures. Together, these indices provided a cross-validated framework, ensuring that rock mass conditions were evaluated from multiple perspectives.

It is important to stress that empirical systems are not predictive models but rather diagnostic tools. They identify relative stability conditions and offer guidance on potential reinforcement requirements, but they cannot substitute for detailed dynamic analyses and numerical modelling.

2.8 Kinematic stability analysis

Kinematic analysis constitutes a cornerstone of preliminary rock slope stability assessment. Originally formalized through the Markland Test (**Markland, 1972**), the method evaluates potential failure mechanisms solely from geometric relationships between discontinuities and slope orientation. Despite its conceptual simplicity, it remains one of the most widely applied approaches in engineering geology, as it rapidly identifies whether the structural configuration of a slope predisposes it to planar, wedge, or toppling failures (**Hoek & Bray, 1981**; **Wyllie & Mah, 2004**).

The principal advantage of kinematic analysis lies in its efficiency: with relatively few input parameters, namely the orientation of discontinuities, slope dip and dip direction, and an estimate of the rock mass friction angle, it yields an immediate diagnostic framework for slope stability. This makes it particularly suited to reconnaissance surveys, hazard screening, and the early phases of slope characterization. Importantly, it does not account for external factors such as groundwater pressure, seismic loading, or stress redistribution, and therefore must be considered as a first-order tool to be complemented by dynamic analyses or more advanced numerical modelling (**Giani, 1992**). Nevertheless, its use is almost universal because it defines the structural conditions under which instability is possible, which is fundamental before addressing whether it is probable.

In the context of this research, structural discontinuity data were obtained through an integrated workflow. Direct field measurements were carried out at accessible and representative outcrops, capturing all the necessary information. However, given the limitations of direct surveys in hazardous or inaccessible sectors, additional information on discontinuities were also extracted from high-resolution 3D point clouds generated via TLS and UAV photogrammetry.

These datasets were analyzed in Agisoft^{TM} Metashape and CloudCompare. For example, using the plugin's Plane Tool of CloudCompare, dip and dip direction values of

joints were obtained by selecting a region of the point clouds and applying a least-squares regression to compute the orientation of the best-fit plane (**CloudCompare, 2024**). By extending structural mapping into otherwise unreachable surfaces, this method reduced sampling bias and enhanced the representativeness of the structural dataset, in line with recent advances in digital outcrop modelling (**Riquelme et al., 2014**; **Gigli & Casagli, 2011**).

The combined dataset, encompassing both traditional field measurements and digital extractions, was processed through stereographic projection. In this framework of the slope stability kinematic analysis:

- planar failures were considered feasible where a discontinuity dipped out of the slope face at an angle greater than the friction angle but lower than the slope dip;
- wedge failures are considered when the line of intersection between the two discontinuity surfaces is steeper than the friction angle and dips out of the slope face;
- toppling failures are assessed when the discontinuity surfaces are sufficiently inclined to allow layer-on-layer sliding, they have the same direction as the slope or in any case differ from it by ± 30°, they dip towards the opposite side of the slope, and this last is sufficiently inclined.

The Markland Test was applied to the Paglicci cave and Vecchiano case studies to identify these potential slope stability conditions.

The results of the kinematic analysis provided a first-level assessment of the structural predisposition to failure across the investigated slopes. While inherently conservative, since it assumes no external triggering factors, the method proved fundamental in guiding subsequent stages of analysis. Specifically, it informed the numerical modelling, ensuring that the most critical orientations and failure scenarios identified in the stereographic domain were explicitly tested under engineering-geological conditions.

Thus, in the workflow of this thesis, kinematic analysis acted as a bridge between geological survey and advanced slope stability modelling, providing both a diagnostic of structural control and a framework to prioritize instability mechanisms for detailed evaluation.

2.9 Limit equilibrium slope stability analysis

To complement the kinematic slope stability assessment, limit equilibrium analyses (LEM-Limit Equilibrium Method) were performed using the Rocscience software RocPlane, SWedge, and RocTopple, each tailored to a specific failure mode. These programs are grounded in classical rock slope engineering concepts and have been extensively verified against analytical formulations and case studies.

RocPlane evaluates planar sliding instabilities by modelling translational slip along discontinuities striking approximately parallel to the slope face. Its formulation builds on shear strength criteria for rock joints (**Barton, 1973, 1977**; **Barton & Choubey, 1977**) and on the principles outlined in rock slope engineering (**Hoek & Bray, 1981**). Later refinements, including the JRC–JCS model (**Barton & Bandis, 1990**) and the developments by **Froldi (1996)**, further consolidated its theoretical background. RocPlane allows both deterministic and probabilistic assessments, with options to incorporate groundwater pressure, pseudo-static seismic coefficients, and reinforcement design.

SWedge extends the dynamic analysis to three-dimensional wedge failures formed by the intersection of two discontinuities with the slope surface. The method is grounded in block theory (**Goodman & Shi, 1985**) and classical limit equilibrium formulations (**Hoek & Bray, 1981**), with stochastic capabilities supported by probabilistic sampling techniques (**Iman et al., 1980**; **Evans et al., 1993**). SWedge can account for hydrogeological conditions, external loads, and seismic forces, and it includes functionalities for bolt and surface support.

RocTopple addresses block toppling instabilities, building on the classical formulations of **Goodman & Bray (1976)** and **Hoek & Bray (1981)**, and it incorporates more recent block-flexure toppling approaches (**Amini, Majdi, & Veshadi, 2012**). It supports deterministic safety factor calculations as well as probabilistic and sensitivity analyses, allowing uncertainty in geomechanical input parameters to be explicitly considered. Hydrogeolog-

ical and seismic effects, along with different support options, can also be simulated.

In this research, potentially unstable volumes were first identified through visual inspection of high-resolution geomatic products, including UAV-derived orthophotos, TLS-UAV-derived point clouds, and dense DSMs. The identified blocks and wedges were subsequently deterministically tested with RocPlane, SWedge, and RocTopple under both static and pseudo-static conditions. The combined application of these programs provided quantitative estimates of their Factors of Safety. This approach is more comprehensive than kinematic checks alone, as it allowed the inclusion of forces such as groundwater and seismic effects. Nonetheless, since seismic loading is treated as an equivalent static force, this stage remains pseudo-static rather than fully dynamic. It therefore represents an essential intermediate step between preliminary kinematic screening and advanced continuum- or discontinuum-based numerical modelling (e.g., FEM, DEM).

2.10 Numerical modeling

Numerical modelling simulates real-world systems using mathematical models to find solutions to complex problems that are difficult or impossible to solve analytically. It involves using numerical methods, such as the Finite Element Method (FEM) or the Finite Difference Method (FDM), to discretize equations and solve them through repeated calculations. Numerical modelling is valuable for investigating scenarios, and its advantages include reducing simulation time and allowing for the easy observation of changes in material parameters once the model is validated.

The Finite Element Method (FEM) represents one of the most established numerical approaches for slope stability analysis, widely adopted in both engineering practice and academic research. Unlike traditional limit equilibrium methods, which require a priori assumptions about failure surfaces, FEM provides a continuum-based framework that allows failure mechanisms to emerge naturally from the stress–strain behavior of the model.

Its applications span from the design of engineered slopes and embankments to the analysis of natural rock and soil slopes, where complex geological, hydrogeological, and loading conditions must be considered.

The principle of FEM lies in discretizing the slope into a finite number of elements, within which equilibrium equations are solved numerically under prescribed boundary conditions.

In geotechnical engineering, the most common approach to evaluate stability is the Strength Reduction Method (SRM), where the shear strength parameters of the material (e.g., cohesion and friction angle) are progressively reduced until the model reaches non-convergence. The reduction factor at which instability occurs defines the Factor of Safety (FoS). This procedure, first formalised by **Griffiths and Lane (1999)** and **Dawson et al. (1999)**, has become the standard framework for numerical slope stability assessment.

Modern implementations of FEM integrate advanced constitutive models, groundwater flow coupling, and dynamic loading, enabling the simulation of both short-term and long-term slope responses.

Rocscience RS3 software, used in this research, provides a powerful three-dimensional environment in which heterogeneous lithologies, anisotropic materials, and complex geometries are represented. Compared to two-dimensional analyses, RS3 allows for a more realistic assessment of slopes influenced by three-dimensional effects such as irregular topography or lateral constraints.

Recent studies highlight ongoing developments in FEM-based slope stability. **Hammah et al. (2005)** extended SRM to non-linear rock mass criteria such as Hoek–Brown, while **Zheng et al. (2006)** clarified alternative definitions of the Factor of Safety within numerical frameworks. More recently, **Dyson & Griffiths (2024)** and **Sysala et al. (2025)** introduced more efficient computational strategies for large-scale three-dimensional problems, and **Huang et al. (2025)** explored probabilistic formulations of FEM, applying them to the system reliability analysis of earth-rock dams.

The advantages of FEM are considerable: it can accommodate complex geometries and stratigraphies, integrate groundwater and seismic effects, simulate staged excavation and reinforcement, and provide both a Factor of Safety and insights into progressive deformation and stress redistribution.

However, limitations remain. FEM requires detailed input parameters, which are often difficult to obtain in situ, and results may be sensitive to mesh design, boundary conditions, and constitutive model selection. Large three-dimensional models can also be computationally demanding, and FEM may not fully capture blocky, discontinuous failure mechanisms, where Distinct Element Method (DEM) approaches are more appropriate.

In this thesis, FEM modelling was performed using RS3 (**Rocscience Inc.**) at Sabereebi and Grotta Paglicci. At Sabereebi, RS3 was used to analyse the stability of the sandstone cliffs hosting the monastic complex, integrating field-derived engineering-

geological parameters and fracture orientations. At Paglicci, FEM modelling supported the assessment of the limestone escarpment above the cave entrance, combining stratigraphic data, joint measurements, and numerical simulations to evaluate potential instability mechanisms.

These applications demonstrate the versatility of FEM in addressing both natural and cultural heritage contexts, providing a robust framework for slope stability assessment that complements field surveys and monitoring data.

2.11 Persistent Scatterer Interferometry (PSI)

Persistent Scatterer Interferometry (PSI) is a multitemporal InSAR technique that measures ground displacements with millimetric accuracy by exploiting radar targets that remain phase-coherent over long time periods. It was originally developed as an evolution of differential SAR interferometry (**Ferretti et al., 2001**; **Hooper et al., 2004**), focusing on persistent scatterers that can be reliably tracked across an image stack. By mitigating temporal decorrelation and atmospheric artefacts, PSI is particularly suited to long-term monitoring of slope instabilities and ground deformation processes, especially where in-situ instruments cannot provide wide spatial coverage (**Crosetto et al., 2016**; **Jia & Liu, 2016**).

In this research, PSI was adopted as a complementary method to TLS and RTS monitoring, providing both spatially extensive coverage and multi-year temporal resolution in areas not visible from the RTS. The analysis was conducted using Sentinel-1 SAR data processed with the SNAP– StaMPS toolchain. SNAP, developed by the European Space Agency (**ESA, 2020**), was used to perform the initial steps, including precise orbit application, radiometric calibration, coregistration of the image stack, interferograms generation, coherence estimation, and removal of the topographic phase using a digital elevation model. The interferometric products were then exported in a format compatible with StaMPS. Within StaMPS, persistent scatterer candidates were identified according to amplitude stability and refined iteratively through phase analysis. Corrections were applied for orbital errors and the atmospheric phase screen, followed by phase unwrapping and inversion to obtain displacement time series and mean velocity fields (**Hooper et al., 2007**; **Hooper et al., 2012**).

An additional advantage of this workflow is its adaptability for batch processing in a Linux environment, where Python scripts can efficiently handle large stacks of Sentinel-1 images, ensuring reproducibility and scalability (**Mancini et al., 2021**; **Foumelis et al.,**

2018).

Despite its effectiveness, PSI analysis is subject to limitations. Areas of dense vegetation, steep slopes, or smooth lithologies can reduce scatterer density due to decorrelation, while atmospheric variability and residual phase unwrapping errors may introduce uncertainties. These issues can be partially mitigated through the combined use of ascending and descending geometries, the installation of artificial targets, the application of coherence thresholds to exclude unreliable points, and validation against independent ground-based datasets. By integrating PSI with RTS and static GNSS measurements, a comprehensive and robust monitoring framework can be achieved, capable of capturing both localized and large-scale ground deformation processes.

In this thesis, PSI was used at Vecchiano to monitor the stability of areas located at the top of the slope under study, not visible from the RTS position.

Chapter 3

Case Studies

3.1 Modeling and stability analysis of the rock mass at the Prehistoric Paglicci Cave system (Italy)

The present case study research and results were partially published in the following scientific manuscript: Beltramone, L., Lucia, V. D., Ermini, A., Innocenti, M., Silvestri, D., Rindinella, A., Ronchitelli, A., Ricci, S., Boschin, F., & Salvini, R. (2024). Applying SLAM-Based LiDAR and UAS Technologies to Evaluate the Rock Slope Stability of the Grotta Paglicci Paleolithic Site (Italy). GeoHazards, 5(2), 457–484. https://doi.org/10.3390/geohazards5020024

3.1.1 Introduction

Natural caves, which hold significant anthropological and geological heritage, are often affected by rock instability, limiting accessibility and the safe development of human activities. To overcome these constraints, modern survey techniques are required to assess and map potential geohazards. Hypogeal environments are typically characterized by complex morphologies, which require integrating multiple methods and technologies.

Among the most widely adopted approaches for spatial data acquisition in extensive and articulated caves are LiDAR (Light Detection and Ranging) and digital photogrammetry.

The use of ground-based LiDAR alone for spatial mapping has been documented in numerous case studies worldwide, including the Las Caldas and Penade Candamo caves in Spain (**González-Aguilera et al., 2009**), the Dachstein cave in Austria (**Buchroithner & Gaisecker, 2009**), the Wonderwerk cave in South Africa (**Rüther et al., 2009**), the Parpalló cave in Spain (**Lerma et al., 2010**), the Les Fraux cave in France (**Grussenmeyer et al., 2012**), the Pollera cave in Italy (**Cosso et al., 2014**), the Jenolan and Koonalda caves in Australia (**Zlot & Bosse, 2014**), the Domica cave in Slovakia (**Gallay et al., 2015**), the Elvandi cave in Ecuador (**Basantes et al., 2017**), the Pechersk Lavra cave in Ukraine (**Shults et al., 2019**), and the Grotta Giusti in Italy (**Nocerino et al., 2019**). Nevertheless, one of the major drawbacks of terrestrial LiDAR is the considerable time required for data acquisition, as highlighted in the case of the İnceğiz caves in Turkey (**Büyüksalih et al., 2020**).

Beyond morphological documentation, TLS has also been applied with a geological focus, as demonstrated in several sites: the Santa Barbara cave in Sardinia, Italy (**Canavese et al., 2011**), the Orgnac's cave in France (**Hajri et al., 2009**; **Jaillet et al., 2011**), the Märchenhöhle cave in Austria (**Roncat et al., 2011**), the Pastora cave in Spain (**García Puchol et al., 2013**), the caves of the Ardèche-Chartreuse-Vercors-Bauges Regional Parks in France (**Hoblea et al., 2014**), the Algar do Penico in Portugal (**Silvestre et al., 2015**), and the Grotta A in Italy (**Fabbri et al., 2017**). Other studies have specifically addressed stability issues, including the Sant'Angelo in Criptis cave in Italy (**Garavelli et al., 2021**), the El Mirador volcanic cave in Ecuador (**Rodríguez et al., 2023**), the Coccio cave in Italy (**Cardia et al., 2023**), the Badajo cave in Spain (**Benrabah et al., 2024**), and the Saint Michael cave in Italy (**Cardia et al., 2024**). In these contexts, 3D models of the cavities were produced using LiDAR (**Garavelli et al., 2021**), digital photogrammetry (**Rodríguez et al., 2023**; **Benrabah et al., 2024**), or a combination of both methodologies

(**Cardia et al., 2023, 2024**). Most of these studies relied on traditional methods of rock slope stability analysis, such as kinematic and dynamic approaches based on rock mass characterization, while only a few introduced more advanced techniques like numerical modeling (**Rodríguez et al., 2023**; **Benrabah et al., 2024**).

In recent years, the development of mobile LiDAR systems based on SLAM (Simultaneous Localization and Mapping) has helped overcome the main limitations of static TLS surveys, namely long acquisition times and the need for multiple scanning stations to avoid shadowed areas in complex morphologies. SLAM systems provide broader and faster coverage, facilitate access to remote or hard-to-reach areas, allow for greater versatility, reduce processing time, and enable more efficient data collection (**Blank et al., 2021**; **Giordan et al., 2021**; **Grasso et al., 2023**; **La Scalea et al., 2019**; **Petracek et al., 2021**). In some cases, surveys must also be extended to external areas surrounding the cave, carried out using similar ground-based technologies or unmanned aerial vehicles/systems (UAV/UAS).

Based on these premises, a multi-technique approach was adopted in this study to characterize the geological hazards of the Grotta Paglicci, located in the municipality of Rignano Garganico (Foggia, Italy; Masseriea Paglicci's property). This internationally renowned Paleolithic cave has been the focus of archaeological and paleoanthropological research by the University of Siena for over 50 years, in collaboration with the local heritage authority (Soprintendenza Archeologica, Belle Arti e Paesaggio of the provinces of Barletta-Andria-Trani-Foggia). Despite its importance, Grotta Paglicci had never been analyzed from an engineering–geological perspective, nor had any stability assessment been conducted.

The adopted multi-technique approach consisted of: (i) a topo-cartographic survey, carried out using a Robotic Total Station (RTS) and Global Navigation Satellite System (GNSS) receivers for precise georeferencing; (ii) spatial data acquisition performed through UAV-based photogrammetry for the external slopes and SLAM-based laser scan-

ning for the cave interior. These datasets were complemented by an engineering–geological survey to characterize joint sets and overall rock mass conditions.

The integrated spatial data were subsequently processed in a GIS environment to generate a 3D topographic model of Grotta Paglicci. From this model, several topographic cross-sections were extracted, which proved essential for interpreting fracture system persistence within the rock mass and for estimating the thickness of the overlying rock above different cave chambers. These cartographic products provided the geometric framework for the subsequent stability analyses.

Based on these inputs, a comprehensive stability assessment was undertaken. A kinematic stability analysis was carried out at both the slope scale, considering the three main sectors, and the block scale, where unstable volumes were identified using UAV imagery and the photogrammetric point cloud. For these selected blocks, a dynamic (pseudo-static) analysis was additionally performed to investigate their response under seismic loading. Furthermore, the influence of water infiltration was analyzed to assess its impact on block detachment mechanisms and overall slope stability.

Finally, 2D Finite Element Method (FEM) numerical modeling was applied along representative cross-sections to evaluate the distribution of principal stresses and displacements, providing deeper insights into the mechanical behavior of the slope–cave system.

Given the site's archaeological significance and its potential for future scientific campaigns, the results obtained provide an essential basis for planning remediation and safety measures. The outcomes of the kinematic, dynamic, and numerical analyses are fundamental for preventing and mitigating hazardous events, ensuring both the safety of researchers and the long-term preservation of the cave.

3.1.2 Anthropological and archaeological settings

The archaeological significance of Grotta Paglicci was first recognized in 1955 by Professor Raffaello Battaglia (University of Padova). Preliminary excavations conducted in 1961 and 1963 under the direction of the Natural History Museum of Verona revealed a Paleolithic deposit. From the 1970s onwards, the University of Siena has conducted systematic research in collaboration with the local heritage office (**Palma di Cesnola, 2004a**).

The site includes the present-day cave and a rock shelter, which originally formed part of the same hypogeal system before the collapse of the vault (Figure 3.1).

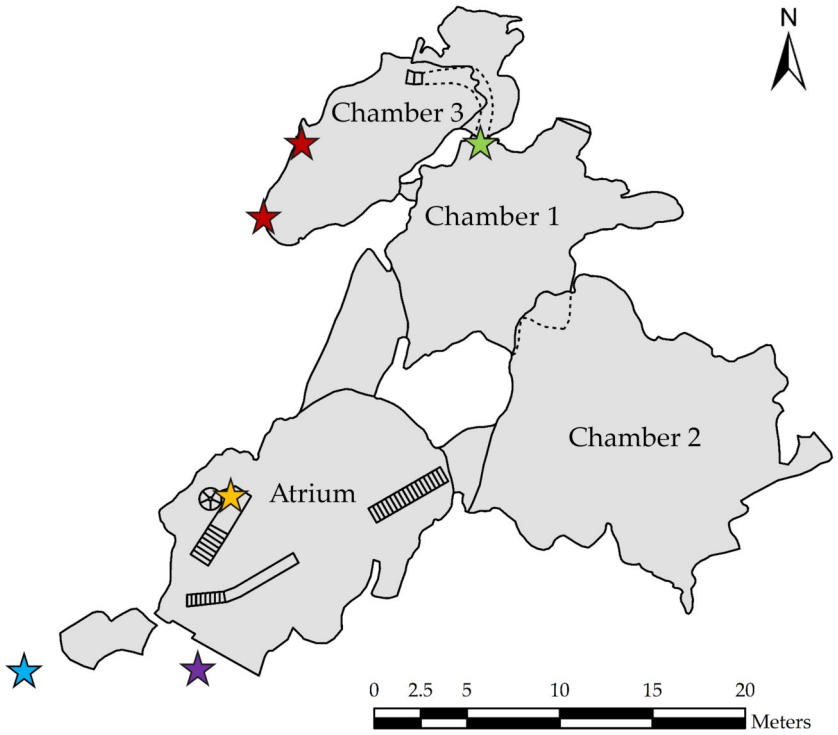

Figure 3.1: Cave system of Grotta Paglicci. Archaeological and anthropological findings are marked with colored stars: yellow = 12-m stratigraphy (Middle–Upper Paleolithic sequence); red = Upper Paleolithic wall paintings; blue = external rock shelter (Lower/Middle Paleolithic); purple = Upper Paleolithic sequence outside the present-day entrance; green = Upper Paleolithic deposit.

Its importance lies in the exceptionally long stratigraphic sequence preserved both

within the cave and within the rock shelter, spanning the Middle and Upper Paleolithic, making it one of the most complete sequences in Europe. Grotta Paglicci is therefore considered a reference site for the Mediterranean region (**Palma di Cesnola, 2004b**).

In the Atrium, a 12-meter-thick stratigraphy was documented (yellow star in Figure 3.1), whose basal layers, attributed to the Middle Paleolithic, partly correlate with deposits preserved in the external rock shelter (blue star in Figure 3.1; **Crezzini et al., 2016**). The Upper Paleolithic sequence ranges from the Aurignacian with marginally backed bladelets (ca. 40,000 years BP) to the Final Epigravettian (ca. 13,000 years BP), encompassing all phases of the Upper Paleolithic known in southern Italy.

The archaeological layers have yielded an extraordinary record of faunal remains, lithic industries, human remains—including two complete Gravettian burials—portable art, and wall paintings that detached from the cave vault (**Arrighi et al., 2008**; **Arrighi et al., 2012a**; **Borgia et al., 2016**; **Dominici et al., 2022**; **Dominici et al., 2023**; **Mezzena & Palma di Cesnola, 1992**, **2004**; **Palma di Cesnola, 2001**, **2006**; **Ricci et al., 2016**; **Ronchitelli et al., 2015**; **Rossini et al., 2022**). Additional finds include one of the earliest pieces of evidence for flour production (**Mariotti Lippi et al., 2015**) and the earliest evidence of domesticated dogs in the Italian Paleolithic (yellow star in Figure 3.1); **Boschin et al., 2020**).

Some layers of the Upper Paleolithic sequence correlate with a thinner deposit immediately outside the present-day cave entrance (purple star in Figure 3.1; **Boscato & Palma di Cesnola, 2005**) and with another stratigraphy found in the inner hypogeal system between Chambers 1 and 3 (green star in Figure 3.1; **Boscato & Palma di Cesnola, 2000**). The deposits are generally rich in anthropogenic traces, although some contexts in both the Atrium and Chamber 1 bear evidence of hyena dens (yellow and green stars in Figure 3.1; **Boscato & Palma di Cesnola, 2000**; **Boscato & Palma di Cesnola, 2005**; **Boschin et al., 2018**).

Finally, Grotta Paglicci preserves unique parietal paintings dating to the Upper Pale-

olithic, located in the inner part of Chamber 3 (red star in Figure 3.1). These represent the only known example of Upper Paleolithic cave art preserved in Italy (**Arrighi et al., 2012b**; **Zorzi, 1964**).

3.1.3 Geological-structural and geomorphological frameworks

The Grotta Paglicci area is located in the western margin of the Gargano Promontory (Figure 3.2C), at the boundary between two major geodynamic–structural domains: to the east, the Apulian Foreland, composed of Mesozoic carbonate platform successions extensively cropping out in the promontory; and to the west, the Bradanic Foredeep basin, represented by the tectonic depression of the Tavoliere delle Puglie, filled with siliciclastic sediments (Figure 3.2A; **Moretti et al., 2011**). This tectonic setting results in a complex geological framework in which carbonate platform units coexist with younger foredeep deposits, forming a transitional zone of significant geological and geomorphological interest.

Limestones are the dominant lithology in the area, with bed thicknesses ranging from 30 to 200 cm and southward dips varying from horizontal to 50–60° (**Moretti et al., 2011**). This lithology belongs to the Monte Calvo del Gargano Member (CBA1 in Figure 3.2B), which dates to the Callovian–Valanginian stages (165.3 ± 1.1–132.6 Ma) (**Spalluto, 2004; Spalluto et al., 2005**). The member forms part of the Calcari di Bari succession, which is Upper Jurassic to Lower Cretaceous in age (201.4 ± 0.2–66.0 Ma).

The Grotta Paglicci area also shows a complex structural history, characterized by ancient strike-slip faults, including the Rignano Garganico and Candelaro faults. These faults have been reactivated with extensional or trans-extensional kinematics and are today partly buried by Quaternary deposits, contributing to the steep escarpments along the southern and southwestern margins of the Gargano Promontory (**Moretti et al., 2011**).

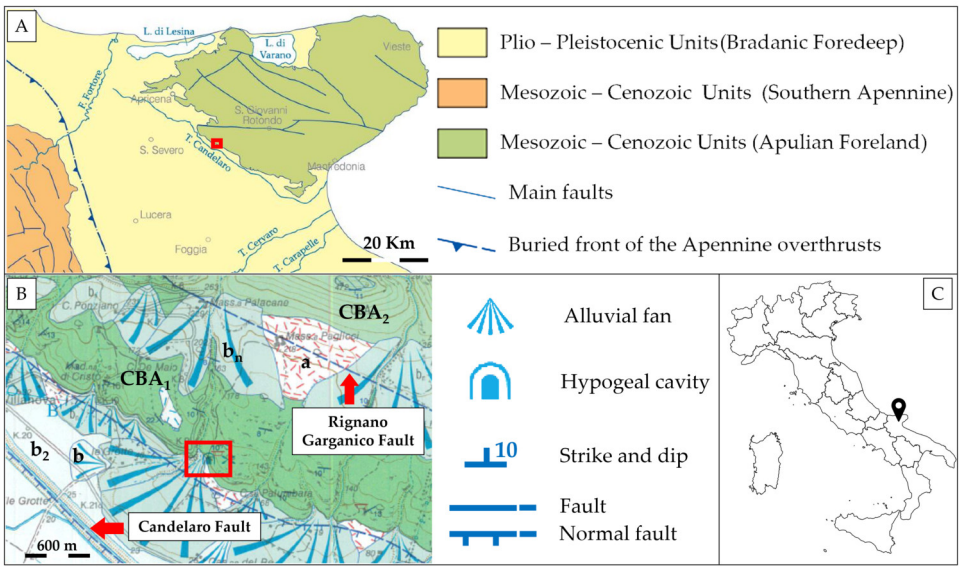

Figure 3.2: Panel (A) The red box highlights the location of Grotta Paglicci in relation to the tectonic framework of the study area (modified from **Moretti et al., 2011**). Panel (B) Geological map with 25 m contour intervals (modified from **Moretti et al., 2011**); lithological units are indicated as follows: a—slope cover deposit, b—present alluvial deposit, b2—colluvial deposit, bn—terrace alluvial deposit, CBA_1—Monte Calvo del Gargano Member, CBA_2—Borgo Celano Member. Panel (C) Inset map showing the position of Grotta Paglicci within the Gargano Promontory.

The predominant morphogenetic process in the Gargano Promontory is karstification, which varies in distribution and shape depending on lithology, structural features, and tectonic evolution (**Cotecchia, 2014**; **Cotecchia & Magri, 1966**). In the study area, two main karst hypogeal cavities are present: Grotta Paglicci and, to the east, the less documented Grotta dei Pilastri. The two are interconnected by a relatively small tunnel, above which a shallow sinkhole has formed, possibly related to the roof collapse. At present, the connecting cavity is inaccessible and filled with collapsed debris, including blocks of various sizes and fine material. Within Chamber 2 of Grotta Paglicci, joints allow minor water inflows and the penetration of root systems from the overlying vegetation, illustrating the close relationship between fracturing, karst evolution, and surface processes.

3.1.4 Seismic framework

The national seismic classification (Figure 3.3A), specifically according to Ordinance P.C.M. no. 3519 of April 28, 2006, divides the territory into four zones, each assigned a different value of the parameter "*ag*", which represents the maximum horizontal peak ground acceleration parameter for soils of Category A (i.e., "*Lithoid formations or homogeneous soils characterized by V_{S30} values greater than 800 m/s, including possible alteration layers up to 5 meters thick*").

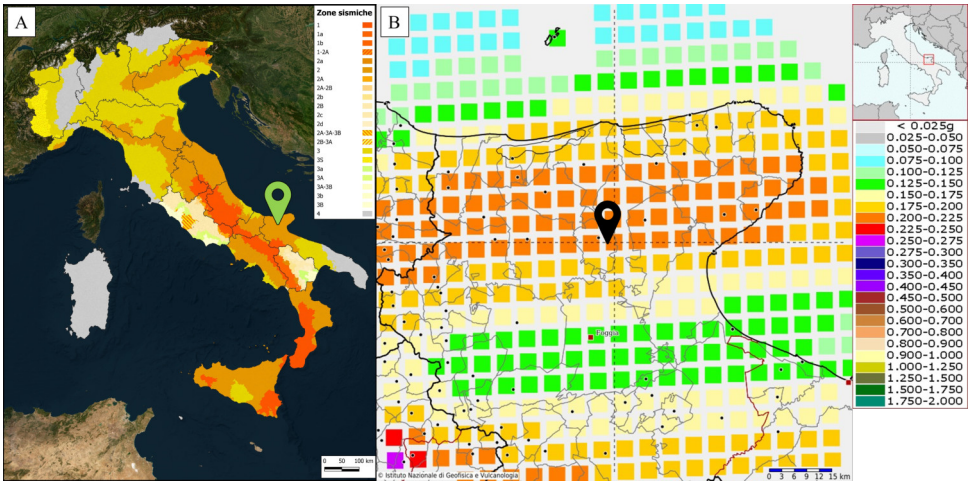

Figure 3.3: Panel (A) shows the "Seismic classification of the Italian territory" updated to 31 March 2023 (Italian Civil Protection Department, `https://rischi.protezionecivile.gov.it/it/sismico/attivita/classificazione-sismica/`); the green pin indicates the location of Grotta Paglicci. Panel (B) shows the seismic hazard model MPS04-S1 for the Gargano area (source: `https://esse1-gis.mi.ingv.it/`); the black pin indicates the location of Grotta Paglicci within node ID 29447.

Through the portal `https://esse1-gis.mi.ingv.it/`, managed by the National Institute of Geophysics and Volcanology (INGV), seismic hazard parameters were defined for node ID 29447, which includes the study area (Figure 3.3B). This area falls within seismic zone 2 – moderate seismicity, associated with Peak Ground Acceleration (PGA) values ranging between 0.200g and 0.250g, with a 10% probability of exceedance in 50 years, referring to Category A soils.

The seismic characterization data provide the necessary seismic coefficients for subsequent dynamic stability analyses of potentially unstable rock volumes defined through UAV high-resolution imagery and point cloud analysis.

The site-specific seismic parameters were obtained using the open portal `https://geoapp.eu/parametrisismici2018/`, which provides values for various Limit States (SLO – Operational, SLD – Damage, SLV – Life Safety, SLC – Collapse Prevention), including horizontal seismic coefficient (k_h), vertical seismic coefficient (k_v), maximum expected horizontal acceleration at the site (A_{max}), and the reduction coefficient of maximum expected acceleration at the site (β). The study type was defined as "*Slope and foundation stability*" with Subsoil Category E, corresponding to "*Soils with characteristics and velocity values equivalent to those defined for Categories C or D, with a substrate depth not exceeding 30m*", and Topographic Category T2, corresponding to "*Slopes with an average inclination $i > 15°$*".

The site-specific seismic parameters used are shown in Table 3.1.

Table 3.1: Seismic parameters for the Grotta Paglicci area.

Type	**Slope and foundation stability**
Subsoil Category	E - Soils with characteristics and velocity values equivalent to Categories C or D, with a substrate depth not exceeding 30m
Topographic Category	T2 - Slopes with an average inclination $i > 15°$
Maximum expected acceleration at the site (m/s^2)	0.250
SLV Coefficients	
$\mathbf{k_h}$ (-)	0.076
$\mathbf{k_v}$ (-)	0.038
$\mathbf{A_{max}}$ **(m/s^2)**	0.250
β (-)	0.240

The adoption of Subsoil Category E was made as a conservative assumption in the absence of direct site-specific geophysical measurements (e.g., Vs_{30}). According to the

NTC (2018), Category E includes soils with mechanical characteristics comparable to Categories C or D, but with a shallow seismic bedrock ($\leq$ 30 m). In the case of Grotta Paglicci, this condition is considered representative of the local setting, where a relatively thin layer of weathered or partially unconsolidated material overlies a carbonate rock substrate fractured and with large internal voids (caves).

Therefore, the classification does not aim to describe the intact rock mass itself, which would be consistent with Category A, but rather the overall mechanical response of the near-surface system controlling the dynamic behavior of the rock mass. Under this perspective, the use of Category E avoids overestimating ground stiffness and provides a precautionary framework for the definition of seismic input parameters in the dynamic stability analysis.

3.1.5 Materials and Methods

To characterize the morphology and structural setting of the Grotta Paglicci area, an integrated survey strategy was adopted, including topographic measurements, UAV photogrammetry, SLAM-based LiDAR acquisitions, and in situ engineering–geological surveys. Rock slope stability was assessed through a multi-step approach combining empirical rock mass classification systems, slope kinematic stability analysis, and dynamic limit equilibrium methods. Finally, 2D FEM numerical modeling was performed to validate these results and provide a continuum-based assessment of the slope.

3.1.5.1 Topographic survey (GNSS and RTS)

To establish a consistent geodetic framework for the study, a topographic survey was performed using both GNSS equipment and an RTS.

A Leica^{TM} GS15 dual-frequency geodetic GNSS receiver and a Leica^{TM} Nova MS50 RTS were employed for this purpose (Figure 3.4A and Figure 3.4B, respectively). Several

types of ground targets were installed, including black–white panels for RTS measurements and scannings (Figure 3.4C), yellow–black panels for UAV imagery acquisitions and georeferencing (Figure 3.4D), and circular optical targets for SLAM-based LiDAR acquisitions (Figure 3.4E).

The GNSS receiver operated in Network Real-Time Kinematic (NRTK) mode, with observation times ranging between 20 seconds and a few minutes, resulting in positional accuracies of ±1 cm horizontally and ±1.2 cm vertically.

Data corrections were provided by the HxGNTM SmartNet service, and the measured points were processed with Leica™ Infinity software (Version 3.4.2; **Leica Geosystems™ AG, 2021**). Using the ConverGo software (**CISIS, 2012**), elevations were adjusted from the WGS84 ellipsoid to mean sea level.

The RTS survey, which was linked to the GNSS framework, allowed the positioning of targets placed on rock walls and other inaccessible surfaces. Even without prisms, the relative accuracy of RTS measurements was estimated between 5 and 8 mm.

In total, thirty control points were acquired and subsequently used to georeference outputs from photogrammetric and LiDAR surveys in the ETRF2000/UTM33N coordinate system.

3.1.5.2 UAV photogrammetric survey

The external slopes and surrounding terrain were mapped through UAV-based photogrammetry using a DJI™ Mavic 2 Pro drone equipped with a Hasselblad® L1D-20C camera (1-inch sensor, 20 MP, 10.26 mm lens).

The survey consisted of three flights: the first was conducted in automated mode with nadir-oriented imagery, planned in UgCS software (Version 4.18; **SPH Engineering, 2023**). The other two flights were executed manually, capturing oblique images at angles between 45° and 65°, almost orthogonal to the slopes, to achieve optimal coverage of vertical rock faces. In total, 550 photographs were collected over approximately 1.9 ha,

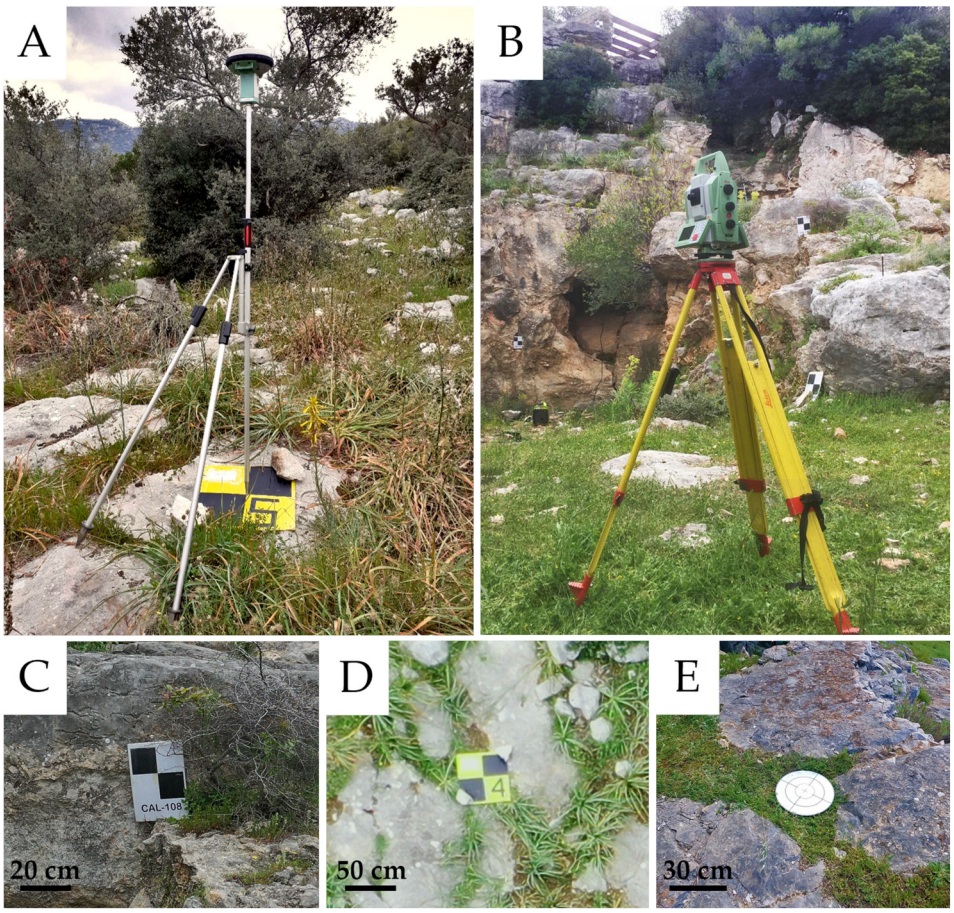

Figure 3.4: Illustrative examples of the different survey stages and targets: GNSS survey (A), RTS survey (B), black–white target for RTS scanning (C), yellow–black target for UAV photogrammetry (D), and circular optical target for SLAM-based LiDAR acquisitions just outside the entrance cave (E).

with a GSD-Ground Sampling Distance close to 1 cm. Flight planning ensured adequate overlap and sidelap of 75%.

For nadiral acquisitions, 12 artificial yellow/black targets (50 × 50 cm) were deployed on the ground, of which 9 were used as Ground Control Points (GCPs) and 3 as Check Points (CPs).

For oblique acquisitions, 14 additional reference points were surveyed with the RTS, including 9 black/white targets (20×20cm) and 5 natural points identifiable on vertical rock walls; of these, 11 were used as GCPs and 3 as CPs.

Data processing was performed in Agisoft™ Metashape software (Version 2; **Agisoft LLC, 2023**), which employs Structure-from-Motion (SfM) and Multi-View Stereo (MVS) algorithms for bundle block adjustment, producing a dense 3D point cloud of the surveyed area.

3.1.5.3 SLAM-based LiDAR survey

The internal morphology of Grotta Paglicci was surveyed using a SLAM-based LiDAR mapping technique, with the aim of reconstructing the cave's geometries in detail.

The instrument employed was an Emesent™ Hovermap ST (Figure 3.5, which simultaneously performs localization, mapping, and navigation through an inertial navigation system, allowing dense 3D point clouds to be acquired without the need for GNSS signals. The system operates with a range of 0.40–100 m and can be set in single-return mode (300,000 points/s) or double-return mode (600,000 points/s); for this survey, the latter was adopted to maximize the level of detail.

Figure 3.5: Acquisition stage in Chamber 2 with the Emesent™ Hovermap ST SLAM-based portable LiDAR.

For visualization purposes, the Hovermap unit was also equipped with an action

camera, enabling simultaneous RGB recording. Illumination was ensured with LED lighting during data acquisition, allowing subsequent color attribution to the point cloud and better visualization of the internal surfaces.

The method proved highly effective in capturing the complex morphology of the cave, which extends for approximately 60m and includes large chambers, confined passages, uneven surfaces, and shaded areas.

A total of three runs were performed: the first scan covered the Atrium and Chamber 2; the second scan covered Chamber 1 and Chamber 3 (the one containing a Paleolithic wall art in red ochre, depicting a horse); the third scan included the Atrium and the outer entrance area to record optical targets for georeferencing. Four external targets were measured with GNSS, ensuring absolute positioning of the final model.

The resulting point clouds were co-registered with Trimble^{TM} RealWorks software (Version 12.4; **Trimble^{TM} Inc., 2021**) exploiting Iterative Closest Point (ICP) algorithms.

3.1.5.4 Engineering-geological survey

The engineering-geological survey was carried out in a traditional manner in the area near the cave entrance, considering six circumscribed, accessible, and safe areas, but above all, deemed essential for defining the fracture pattern (Figure 3.6).

This survey made it possible to collect useful information on the lithology characterizing the area and on the engineering-geological characteristics of the discontinuities affecting the rock mass. In particular, data were collected regarding the orientation, spacing, persistence, aperture, type of infilling, roughness (using Barton's comb and classified according to the JRC–Joint Roughness Coefficient parameter), alteration, moisture content, and indirect uniaxial compressive strength (via R rebound value of the Schmidt hammer or sclerometer) of all the discontinuities present, whether fractures or bedding planes of the Monte Calvo del Gargano limestones.

In selecting the scan lines, logistical and anthropological aspects were considered,

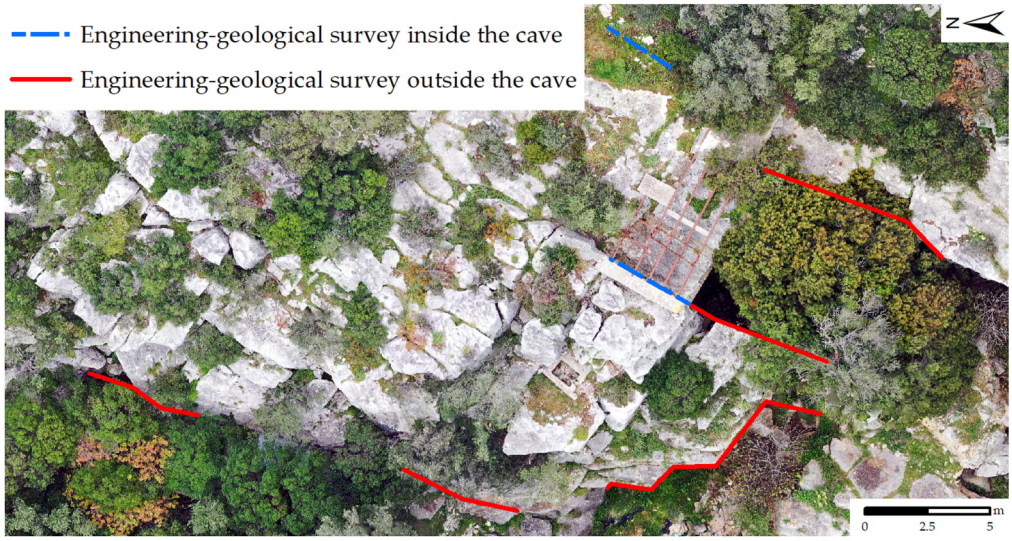

Figure 3.6: Survey scan lines used for the engineering–geological investigation, highlighting the outcrops selected for discontinuity and rock mass characterization.

along with different slope orientations, to ensure subsequent stability assessments could address diverse geometric conditions.

Due to the external morphology of the area, characterized by steps with vertical or sub-vertical walls several meters high, the presence of mixed vegetation—very dense in some areas—the absence of safe paths, and the presence of unstable blocks, it was decided to also carry out surveys inside the cave and to collect further data using photographs and all the georeferenced 3D data obtained from UAV photogrammetry and SLAM-based LiDAR surveys (Figure 3.7). The interpretation, carried out in CloudCompare (Version 2; **CloudCompare, 2021**), allowed the measurement of discontinuity orientation, spacing, and persistence.

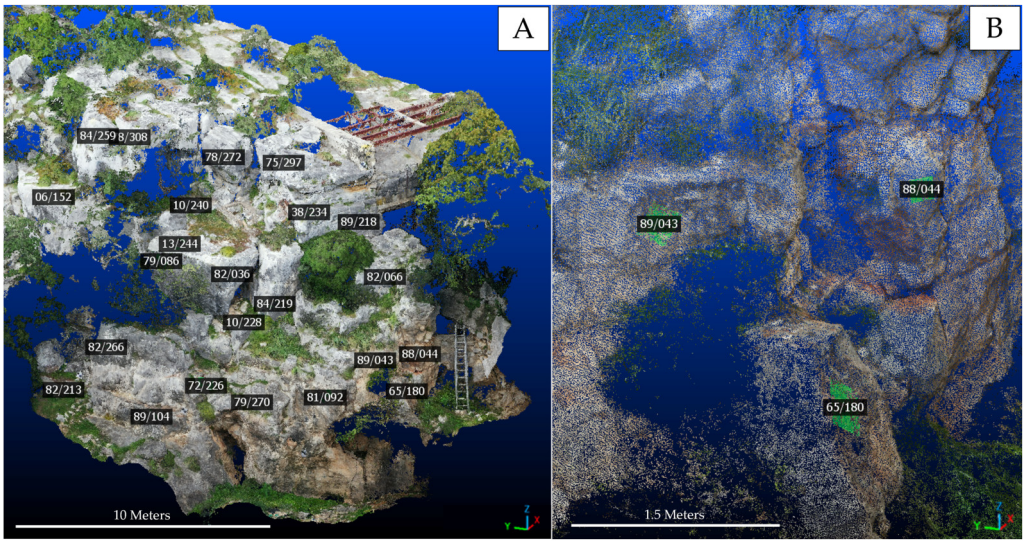

Figure 3.7: Panel A is an example of various discontinuity orientations measured on the 3D point cloud. Panel B is a detail of the same with the surfaces areas used for orientation measurements highlighted with green parallelepipeds.

3.1.5.5 Rock Mass Classification

All the data collected with the in situ engineering-geological surveys, were processed as a whole and used to characterize the rock mass according to the approaches proposed by **Bieniawski (1989 – Rock Mass Rating, RMR)**, **Bar & Barton (2017 – Q-slope method)** and **Romana (1985 – Slope Mass Rating, SMR)**. These empirical rock engineering classification methods are widely applied for defining the characteristics of a rock mass, selecting appropriate support and reinforcement measures, and evaluating the performance of both natural and excavated slopes.

The RMR system enables the characterization of rock masses and, through empirical correlations proposed by **Bieniawski (1989)**, provides estimates of key engineering-geological parameters—such as friction angle (φ), cohesion (c), and deformation modulus (E)—when laboratory testing is not available. Furthermore, the values obtained with the RMR method serve as a fundamental input for the failure criterion adopted in numerical modeling (see Section 3.1.5.6.3).

The SMR method, introduced by **Romana (1985)**, is specifically designed for the stability assessment of rock slopes. It accounts for factors that most directly influence slope stability, including slope height and angle, the orientation and persistence of discontinuities, groundwater conditions, and the intrinsic strength of the rock mass.

The Q-slope method (**Bar & Barton, 2017**) incorporates geological and environmental conditions that can affect slope stability over long time periods. It allows for the identification of a limiting slope dip angle for stability and provides empirical relationships to derive required or acceptable slope angles corresponding to Probabilities of Failure (PoF) of 1%, 15%, 30%, and 50%.

Given the specific features and complementary nature of these three approaches, their combined application in this study was aimed at achieving a comprehensive characterization of the slope stability conditions at Grotta Paglicci.

3.1.5.6 Slope stability analysis

The assessment of slope and cave stability at Grotta Paglicci was carried out through a multi-step approach combining empirical, analytical, and numerical methods. First, a kinematic analysis was applied to identify potential instability mechanisms controlled by discontinuities. Subsequently, a dynamic block analysis was then conducted to simulate the possible detachment and movement of unstable volumes. Finally, the stress–strain response of the rock mass was investigated using two-dimensional finite element modeling (FEM), providing a numerical validation of the overall stability conditions **(Sari, 2019, 2021)**.

3.1.5.6.1 Kinematic stability analysis

The kinematic assessment was carried out using the **Markland Test (1972)**, a stereographic technique that enables the identification of potential failure modes such as planar sliding, wedge sliding, and toppling. The analysis incorporated slope orientations, joint

geometries, and the rock mass friction angle. Moreover, the analysis was performed both at the slope scale and at the block scale, to evaluate possible instability affecting entire slope sectors as well as discrete rock blocks.

Data used for this assessment were derived from both in situ engineering–geological surveys and photointerpretation of geomatic datasets (UAV photogrammetry and SLAM-based LiDAR) (see Section 3.1.5.4).

These datasets provided a statistically significant representation of discontinuity sets, which were then analyzed using Rocscience^{TM} Dips software (Version 8.022; **Rocscience Inc, 2022**). The software employs stereographic projection methods described by **Goodman (1980)**, as well as those of **Hudson & Harrison (1997)**, enabling the evaluation of rock–slope relationships and potential kinematic instabilities.

The results of this analysis were not only fundamental to identifying the most critical slope orientations but also served as input parameters for subsequent SMR (**Romana, 1985**) calculations.

3.1.5.6.2 Limit equilibrium stability analysis

The stability of potentially unstable rock blocks was deterministically assessed through limit equilibrium analyses using Rocscience^{TM} software (RocPlane, SWedge, RocTopple; **Rocscience Inc, 2022, 2023**). Based on discontinuity data derived from engineering–geological surveys and 3D photogrammetry–LiDAR products, the deterministic dynamic analysis was conducted by adopting the Barton–Bandis shear strength criterion (**Barton & Bandis, 1990**). It accounts for the mechanical behavior of discontinuities as a function of their roughness, wall strength, and residual friction. In particular, the parameters considered were (Table 3.2): the Joint Roughness Coefficient (JRC), describing the surface irregularity of the discontinuities; the Joint Wall Compressive Strength (JCS), expressing the compressive strength of the rock wall material; and the residual friction angle (ϕ_r) of the joint surfaces.

Table 3.2: Values of JCS, JRC, and φ_r used for the characterization of discontinuities considered in the deterministic dynamic analysis of the identified blocks.

Parameter	**Bedding**	**S1**	**S2**	**S3**
JCS (MPa)	33.35	36.52	41.86	34.90
JRC	10–12	10–12	12–14	12–14
φ_r (°)	29	30	32	29

These parameters were derived from the results of the engineering–geological survey (e.g., Schmidt hammer rebound values, Barton's comb measurements) and literature data for the local lithologies.

In addition, the dynamic analysis was carried out following the provisions of Eurocode 7 (**Frank et a., 2004**) for jointed rock slopes. Approach 1 – Combination 2 was adopted, applying the partial factors defined in the code (Table 3.3).

Table 3.3: Partial factors defined by Eurocode 7 EN 1997 for Approach 1 - Combination 2.

Eurocode 7: Approach 1 - Combination 2	**Partial Factor**
Effective cohesion	1.25
Shear strength coefficient	1.25
Unit weight	1.00
Shear strength (other models)	1.25
Seismic coefficient	1.00
Pore water pressure	1.00

The analyses were performed under four main conditions: (i) standard conditions (no water, no seismic input); (ii) presence of water along the discontinuities, expressed as different percentages of infilling; (iii) seismic loading, using the local coefficients k_h = 0.076 and k_v = 0.038; and (iv) combined presence of water and seismic input.

This dynamic stage provided a more comprehensive evaluation than kinematic checks alone, while serving as an intermediate step toward advanced numerical modelling.

3.1.5.6.3 Numerical modeling

The numerical modelling of Grotta Paglicci was carried out using RS2^{TM} software (Version 11.019; **Rocscience^{TM}, 2023**), building upon the results of the kinematic stability analysis to evaluate the principal stresses, expected displacements, strength factors, and strain distribution within the rock mass. The site was characterized as a slightly jointed limestone formation, with three main joint sets in addition to the bedding planes. Although discrete element methods have traditionally been preferred for such discontinuous rock masses, recent research has demonstrated that finite element methods (FEM) can provide equivalent and reliable results (**Sari, 2021**).

The numerical models were constructed by integrating external and internal 3D point clouds of the cave, which enabled the identification of morphological features required for the extraction of representative cross-sections. These sections (AA', BB', and CC') were created in CloudCompare, digitized in a CAD environment, and subsequently imported into RS2^{TM} in DXF format (Figure 3.8).

Their orientation was selected to analyze key directions inside the cave, independent of those considered in the SMR and kinematic stability assessments.

The 2D numerical modelling followed a multi-step procedure. Initially, a control point grid was generated using the available topographic data, which served as the basis for constructing a surface mesh of the cave's overall geometry. This mesh was further discretized into smaller elements to enhance accuracy, particularly in the areas considered most critical. After defining the mesh, the relevant geotechnical properties—such as rock strength, internal friction angle, and cohesion—were assigned to reproduce the cave's geological characteristics.

Incorporating geotechnical parameters into a 2D model is essential to simulate how the material deforms, withstands shear stresses, and interacts with both water and surrounding materials, thereby ensuring conditions that closely resemble reality. This process is

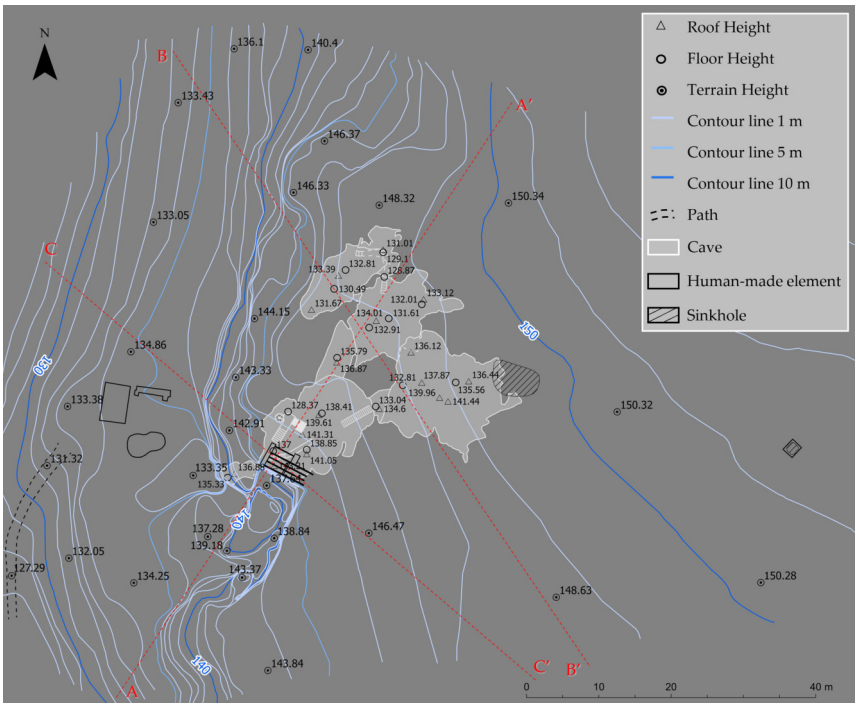

Figure 3.8: New topographic map of the study area from the processing of photogrammetric and SLAM-based LiDAR mapping techniques. Red letters and dotted lines represent the cross-sections used in 2D numerical modeling.

also fundamental for achieving reliable assessments of slope stability, deformation, and potential failure mechanisms.

Geotechnical parameters such as unit weight (MN/m^3), Poisson's ratio, and tensile strength refer to local technical documentation (**Geogar, 2015**; **Italferr, 2015**), while values such as cohesion (c), friction angle (φ), and Young's modulus (E) were derived from empirical formulations based on the RMR classification (**Bieniawski, 1989**). The rock mass was modeled as drained, isotropic, with loading conditions limited to body forces due to the absence of in situ stress measurements. Table 3.4 summarizes the parameters for the 2D modelling.

Table 3.4: Engineering–geological attributes of the modeled rock material.

Parameter	**Value**
Material Name	Monte Calvo del Gargano member
Material Color	
Initial Element Loading	Body Force Only
Unit Weight (MN/m^3)	0.0225
Elastic Type	Isotropic
Poisson's Ratio	0.30
Young's Modulus E (MPa)	34,000
Failure Criterion	Mohr–Coulomb
Material Type	Elastic
Peak Tensile Strength (MPa)	0.053
Peak Friction Angle φ (°)	38
Peak Cohesion c (MPa)	0.335
Material Behavior	Drained
Porosity Value (%)	0.5
Static Water Mode	Dry

The green color refers to the limestones of Monte Calvo del Gargano member as shown in the numerical models.

The geotechnical models incorporated the principal discontinuity sets, including their orientation, spacing, and persistence. These parameters were determined through a combination of traditional field surveys and geomatic analysis, the latter based on UAV photogrammetry and SLAM-based LiDAR scanning, covering both the external rock walls and the internal cave chambers. For the stability assessment, the Barton–Bandis failure criterion was adopted (**Barton & Bandis, 1990**). This criterion, which has been extensively validated for a wide range of rock types and geological contexts, allows for the definition of discontinuity shear strength as a function of the Joint Roughness Coefficient (JRC), derived directly from the engineering–geological survey. Additional input parameters, including Joint Wall Compressive Strength (JCS), residual friction angle (φ_r), and normal (k_n) and shear stiffness ($k_{s)}$ values, were calculated using empirical relationships established in previous studies (**Barton & Choubey, 1977**; **Barton, 1973**; **Miller, 1965**).

The engineering–geological properties assigned to the discontinuities are summarized in Table 3.5.

Table 3.5: Engineering–geological characteristics of the discontinuity systems.

System	**Color**	**Normal Stiffness (MPa/m)**	**Shear Stiffness (MPa/m)**	**JCS (MPa)**	**JRC**	**Residual Friction Angle (°)**
S1		79,610	30,619	36.52	11	30
S2				41.85	13	32
S3				34.90	13	29
Bedding				33.35	11	29

The colors refer to the different discontinuity systems as shown in the numerical models.

Figures 3.9, 3.10, and 3.11 show the geotechnical models created with RS2^{TM} software (Version 11.019; **Rocscience^{TM} Inc. 2023**) using the geometric information derived from the AA', BB', and CC' sections, respectively. The finite element analysis of the three cross-sections was conducted iteratively, with computations continuing within a certain maximum number of iterations and up to reaching numerical convergence.

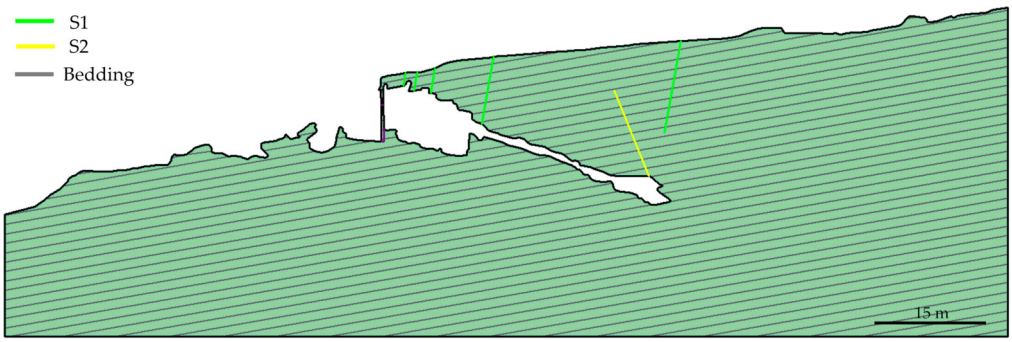

Figure 3.9: AA' cross-section; the green and yellow lines represent the main identified joints, while the gray lines indicate the limestone bedding.

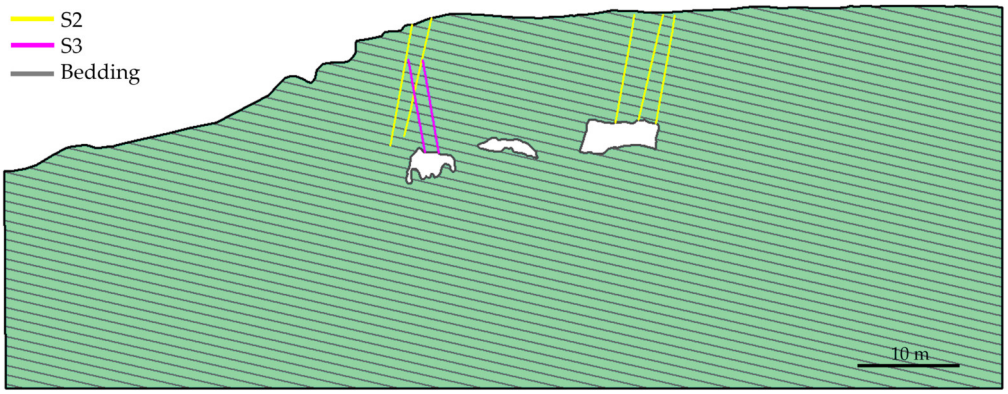

Figure 3.10: BB' cross-section; the yellow and magenta lines represent the main identified joints, while the gray lines indicate the limestone bedding.

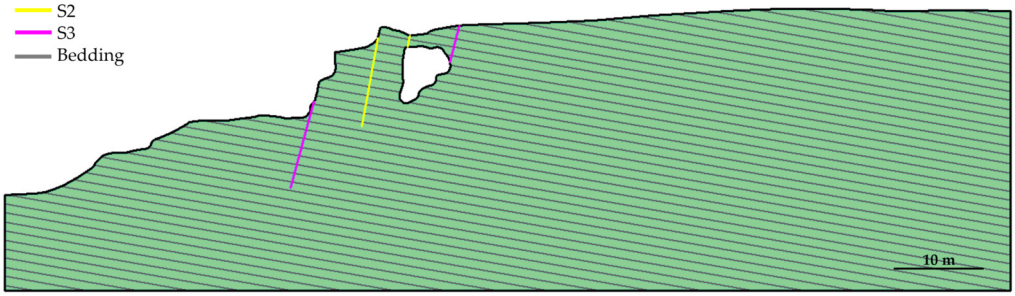

Figure 3.11: CC' cross-section; the yellow and magenta lines represent the main identified joints, while the gray lines indicate the limestone bedding.

3.1.6 Results

3.1.6.1 SLAM-based point cloud coregistration and georeferencing

The integration of the three SLAM-based LiDAR surveys produced a georeferenced 3D point cloud (Figure 3.12). The process relied on four Ground Control Points (GCPs), identified by circular optical targets, which allowed georeferencing in the absolute reference system ETRF2000/UTM33N. The estimated georeferencing accuracy was approximately 6cm.

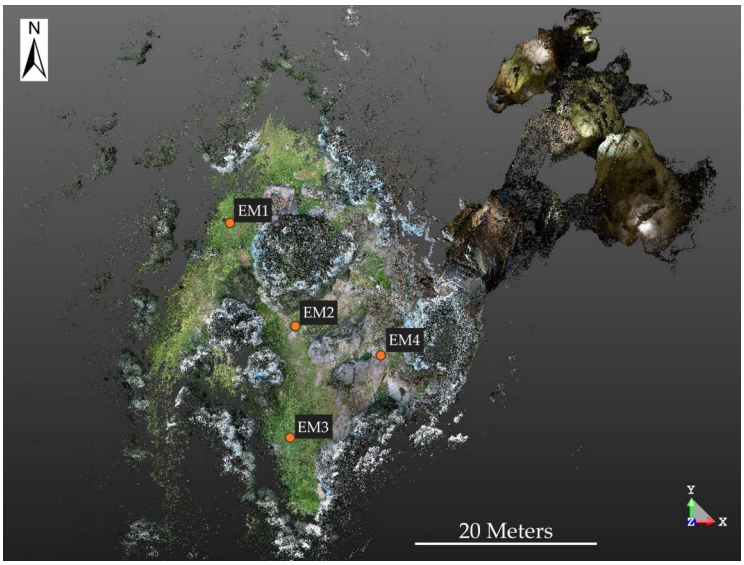

Figure 3.12: (A) Nadiral view of the georeferenced 3D point cloud from SLAM-based LiDAR surveys. Orange dots (EMn) indicate the GCPs used for georeferencing.

3.1.6.2 UAV photogrammetric data processing

Using Structure-from-Motion (SfM) and Multi-View Stereo (MVS) algorithms, 1.99 million tie points were extracted for image alignment. The exterior orientation achieved a Root Mean Square Error (RMSE) of 2.9 cm for GCPs and 1.9 cm for CPs. The final 3D dense point cloud contained about 170 million points and was interpolated to generate a digital dense elevation model (DDEM) with a spatial resolution of 1.8 cm/pixel. From the DDEM, ortho-rectified and mosaiced images were obtained (frontal and nadiral views) with a ground sampling distance (GSD) of 1 cm/pixel (Figure 3.13).

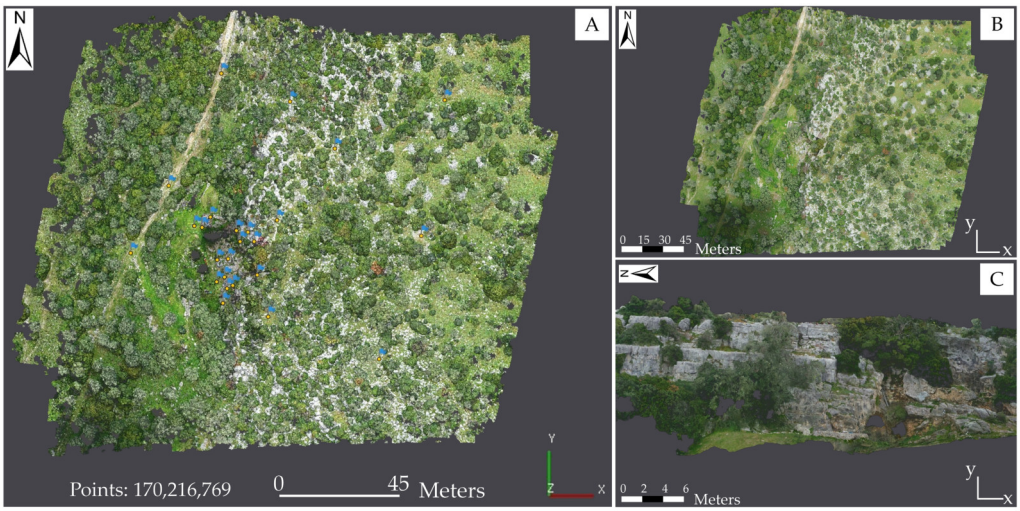

Figure 3.13: (A) Nadiral view of the georeferenced 3D dense point cloud. Blue flags mark the GCPs used for exterior orientation. (B) Nadiral orthophotomosaic. (C) Detail of the frontal orthophotomosaic.

3.1.6.3 Engineering-geological survey

The survey revealed discontinuities with markedly variable orientations. Data obtained from traditional engineering–geological investigations, integrated with photointerpretation of geomatic outputs, enabled detailed rock mass characterization. In total, 364 discontinuities were deterministically measured and evenly distributed across the study area, including sectors at different elevations. This large dataset enabled the identification of the main discontinuity systems, as illustrated in the stereographic projection (Figure 3.14). As summarized in Table 3.6, the main engineering-geological parameters were grouped according to the identified discontinuity systems.

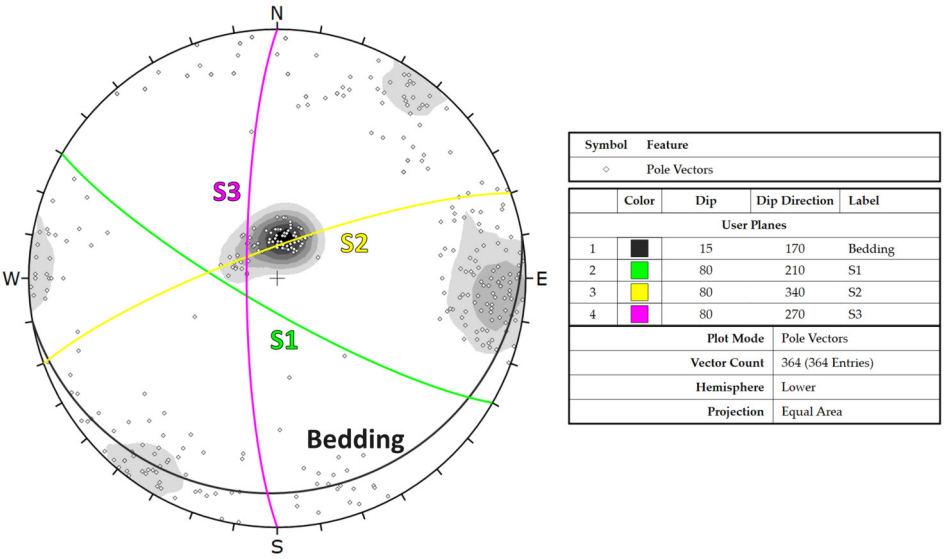

Figure 3.14: Stereographic projection of discontinuities identified through both the in situ engineering–geological survey and the photointerpretation of geomatic datasets. Orientations are expressed as dip and dip direction, following the right-hand rule, and represented with the Schmidt equal-area method (lower hemisphere). Density variations are indicated by different shades of gray.

Table 3.6: Engineering–geological parameters of the identified discontinuity systems.

Parameter	**Bedding**	**S1**	**S2**	**S3**
Dip (°)	15	80	80	80
Dip direction (°)	170	210	340	270
Spacing (m)	0.9	1.2	2.0	1.4
Length (m)	>20	>10	>10	>10
Aperture (mm)	30	13	125	35
Filling (mm, type)	30, cemented limestone	10, debris	125, debris	32, debris
R-value (discontinuity)	26	28	31	27
R-value (intact material)			39	
JRC	10–12	10–12	12–14	12–14
Surface weathering	Moderately weathered	Slightly weathered	Moderately weathered	Moderately weathered
Humidity	Dry	Dry	Dry	Dry

3.1.6.4 Rock Mass Classification

3.1.6.4.1 Rock Mass Rating (RMR) method

According to the approach of **Bieniawski (1989)**, the basic rock mass rating (RMRb) of the investigated formation was calculated as 67, which corresponds to Class II and thus indicates good quality rock mass conditions. From this classification, an indicative estimation of the shear strength parameters was derived using the empirical correlations proposed by **Bieniawski (1989)**, obtaining a cohesion value of 335 kPa, a friction angle of 38°, and a Young's modulus of 34 GPa (Table 3.7).

Table 3.7: Shear strength parameters and deformation modulus (E), calculated according to **Bieniawski (1989)**.

Parameter	**Value**
Cohesion c (kPa)	335
Friction angle φ (°)	38
Young's modulus E (GPa)	34

3.1.6.4.2 Q-Slope method

An additional empirical evaluation of rock mass stability was carried out using the Q-slope method developed by **Bar & Barton (2017)**. The calculated Q-slope value was 0.81. Considering the average slope dip of 80°, the stability chart, in Figure 3.15, indicates critical conditions, confirming a predisposition to potential failure. Table 3.8 reports the slope angles corresponding to different probabilities of failure (PoF), showing that stabilization measures would be required to ensure long-term stability under natural conditions.

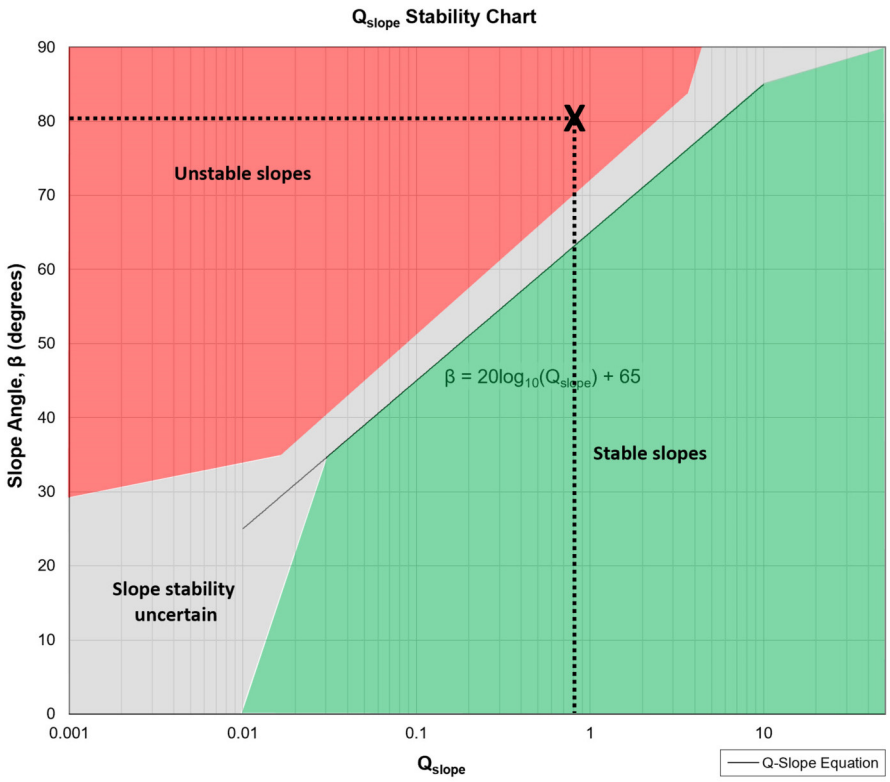

Figure 3.15: Stability chart of the Q-slope method (after **Bar & Barton, 2017**), with the black cross marking the critical stability conditions for an average slope angle of 80°.

Table 3.8: Slope dip angle values required to accept different probabilities of failure (PoF) according to the Q-slope method (**Bar & Barton, 2017**).

PoF (%)	**Slope angle (°)**
1	63
15	66
30	69
50	72

3.1.6.4.3 Slope Mass Rating (SMR) method

The SMR approach proposed by **Romana (1985)** was also applied to further characterize the rock mass by analyzing the relationships between discontinuity orientations and

natural slope geometries. Three slopes (V1, V2, and V3) were examined with respect to planar, toppling, and wedge failure mechanisms (Figure 3.16).

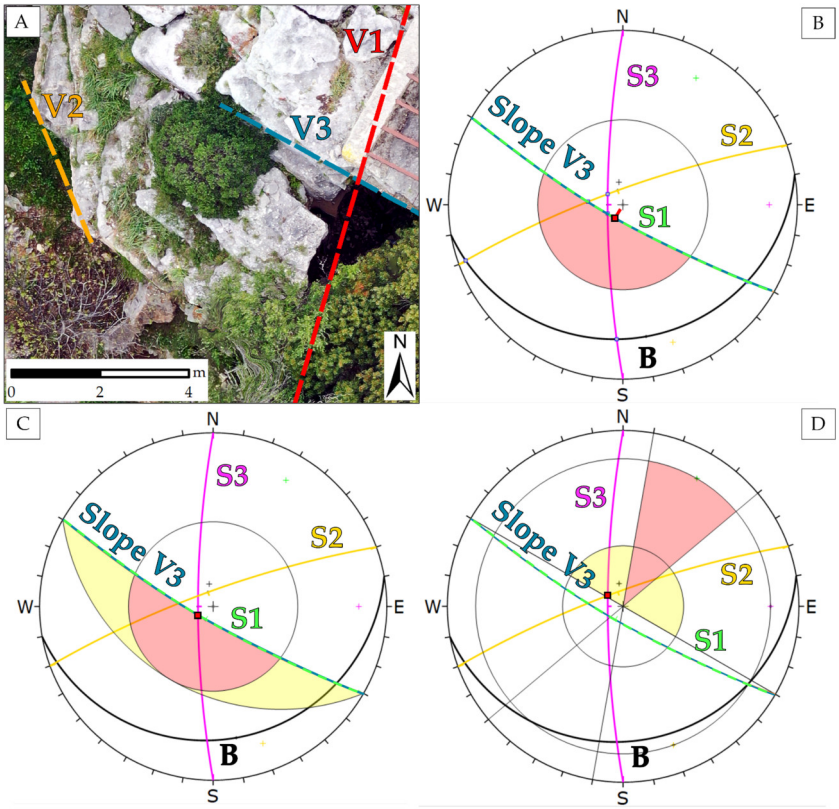

Figure 3.16: Nadiral orthophotomosaic illustrating the orientations of the three slopes (V1, V2, and V3) reported in Table 3.9, which were analyzed using the SMR method (A). On slope V3, examples of kinematic stability assessment are presented through stereographic projections (Wulff equal-angle method, lower hemisphere): planar sliding (B), wedge sliding (C), and direct or oblique toppling (D). The discontinuity sets S1, S2, and S3 correspond to those described in Table 3.9.

Table 3.9: Average values of dip direction and dip of discontinuity systems and slopes used to verify potential instabilities.

System	**Dip Direction/Dip (°)**	**Slope**	**Dip Direction/Dip °)**
Bedding	170/15	V1	285/80
S1	210/80	V2	245/80
S2	340/80	V3	210/80
S3	270/80		